Nanostructured Carbons and Additives for Improvement of the Lithium-Sulfur Battery Positive Electrode

by

Scott Evers

A thesis
presented to the University of Waterloo
in fulfillment of the
thesis requirement for the degree of
Master of Science
in
Chemistry - Nanotechnology

Waterloo, Ontario, Canada, 2013

AUTHOR'S DECLARATION

I hereby declare that I am the sole author of this thesis. This is a true copy of the thesis, including any required final revisions, as accepted by my examiners.

I understand that my thesis may be made electronically available to the public.

_____

Scott Evers

ABSTRACT

Large specific gravimetric/volumetric energy density, environmental benignity and safe low working voltage. All of these points have been used to describe the lithium sulfur (Li-S) battery in the past, but often times it is short cycle life and poor capacity retention that is associated with the Li-S battery. In order to realize the full potential of the Li-S battery in society today, many obstacles must be overcome. In a typical Li-S cell with an organic liquid electrolyte sulfur is reduced by lithium during discharge and subsequent lithium polysulfide species (Li_2S_x where x, $2 < x < 8$) are formed. These species are readily soluble in typical organic electrolytes and can lead to low Coulombic efficiency and most challenging: active mass loss. Through the loss of active mass, rapid capacity fading occurs over long-term cell cycling. Overcoming the loss of active mass and stabilizing cell capacity at high rates is pivotal to the realization of practical Li-S cells. In this thesis, four separate concepts and materials were studied and prepared with the aim to improve the Li-S batteries capacity, cycle life and capacity retention.

In the first part, reduced graphene oxide is used as both a conductive additive and a host material for a sulfur positive electrode to limit polysulfide dissolution into the electrolyte. Graphene sulfur composite (GSC) was prepared by an easily scalable one-pot synthetic technique. Graphite oxide was first exfoliated by sonication and was then mixed with a solution of sodium polysulfides. Acid oxidation of this solution forms sulfur particles that are enveloped by slightly reduced graphene oxide sheets. GSC has an open architecture for facile lithium ion diffusion and the reduced graphene oxide coating provides electrical conductivity as well as hydrophilicity that can retain hydrophilic lithium polysulfides. Through the use of lightweight, high surface area reduced graphene

oxide; the GSC contains the highest ever reported sulfur content of 87 wt%. In a Li-S battery, GSC shows good electrochemistry with an initial specific discharge capacity of 705 mA h g^{-1}_{sulfur} at a discharge rate of C/5 (full discharge in 5 hours). The cells capacity fades slightly over 50 cycles and the cause of this is most likely the formation and isolation of the final discharge product Li_2S at the positive electrode.

The second part addresses the issue that mesoporous carbons are effective at retaining lithium polysulfides through containment in a nano-framework; however, dissolution still remains a problem that can lead to significant capacity fading. In this work, a mesoporous carbon with 12 nm pores was infiltrated with 60 wt% sulfur and showed poor electrochemistry with a loss of 55% capacity after only 100 cycles. To improve capacity retention and limit polysulfide dissolution, mesoporous titania was added to the sulfur/mesoporous carbon positive electrode. The mesoporous titania is electrochemically inactive and only acts to sorb lithium polysulfides that have escaped from the mesoporous carbon and hinder them from leaving the positive electrode matrix. Lithium polysulfides are attracted to titania because of hydrophilic-hydrophilic interactions, but are easily desorbed near the end of reduction and return to the conductive mesoporous carbon to be further reduced. With the addition of only 4 wt% mesoporous titania additive, there was significant improvement in capacity retention (82% after 100 cycles) and a decrease in polarization in the cell which translates into a larger cell energy density.

In the third part, a new hollow spherical carbon is synthesized with a mesoporous shell that allows lithium ion transfer, but limits polysulfide dissolution into the electrolyte. Porous carbon spheres (PCS's) are synthesized by first preparing uniform solid silica spheres and then coating these spheres with a resorcinol/formaldehyde polymer. The

porosity in the shell is introduced through the addition of a cationic polymer in the resorcinol/formaldehyde polymer that is eliminated when the material is carbonized. The interior silica is removed by etching and sulfur is then impregnated into the porous shell through a simple melt-diffusion method. The PCS's filled with 68 wt% sulfur exhibit extremely stable cycling with capacity retention over 100% after 100 cycles at a super high rate of 1C. The PCS's allow uniform lithium diffusion throughout the positive electrode and are also able to retain the polysulfides in the interior of their cores and walls.

The fourth and final part introduces the use of carbide derived carbons (CDC's) as hosts for sulfur in a Li-S battery. CDC's are prepared by chlorine treatment of metal carbides whereby the metal atom is removed as a gaseous metal chloride, leaving micropores in the carbon structure. The micropores could act to confine sulfur molecules and limit their dissolution in the electrolyte upon being reduced to lithium polysulfides. Two different particle sizes of CDC's were used with the nano-CDC producing better electrochemical results than the bulk-CDC. However, to obtain the best electrochemistry a new vapour-infusion technique was required to infiltrate sulfur into the micropores in the gas phase. Overall, it was determined that the lack of hydrophilic functional groups in the CDC reduced its ability to retain lithium polysulfides and thus did not perform well as a Li-S battery positive electrode.

ACKNOWLEDGEMENTS

I would like to extend my appreciation to my supervisor, Professor Linda F. Nazar, for her guidance throughout the course of this research project.

I would also like to extend my appreciation to other members of the research group past and present that have lent me their assistance and expertise: Dr. Xiulei Ji, Dr. Marine Cuisinier, Dr. Guerman Popov, Dr. Guang He, Dr. Brian Ellis, Dr. Taeeun Yim, Robert Black and Brian Adams.

TABLE OF CONTENTS

LIST OF FIGURES

LIST OF TABLES

GLOSSARY

AAO	Anodized alumina membrane
AC	Activated carbon
AC	Alternating current
AF	Agitation-friction
BET	Brunauer-Emmett-Teller
BJH	Barrett-Joyner-Halenda
BMC	Bimodal mesoporous carbon
CDC	Carbide derived carbon
CNF	Carbon nanofiber
DCNT	Disordered carbon nanotube
DME	1,2-dimethoxyethane
DOL	1,3-dioxolane
FTIR	Fourier transform infrared
GO	Graphene oxide
GSC	Graphene-sulfur composite
HF	High frequency
IR	Infrared radiation
Li-S	Lithium sulfur
MC	Mesoporous carbon

MD	Melt-diffusion
MWCNT	Multi-walled carbon nanotube
OCV	Open circuit voltage
PCS	Porous carbon sphere
PEGDME	Poly(ethylene glycol) dimethyl ether
PSD	Pore size distribution
PVdF	Polyvinylidene fluoride
PXRD	Powder X-ray diffraction
QSDFT	Quenched solid density functional theory
rGO	Reduced graphene oxide
SCM	Silica colloid monolith
SEM	Scanning electron microscope
STEM	Scanning transmission electron microscope
TEGDME	Tetraethylene glycol dimethyl ether
TEM	Transmission electron microscope
TFSI	Bis(trifluoromethylsulfonyl)imide
TGA	Thermogravimetric analysis
VI	Vapour-infusion

Chapter 1

Introduction

1. Overview of Lithium-Sulfur Batteries

In the next 25 years energy demand will increase by at least 35% from our present usage with the consumption of fossil fuels slated to grow, not decline. This will put increasing pressure on the world's reserves of non-renewable energy sources and will also greatly affect climate disruption. Electrical energy storage systems can allow more widespread use of intermittent renewable energy generators (wind, solar, wave), and reduce the consumption of fossil fuels for transportation. Conventional lithium-ion (Li-ion) batteries utilize a positive electrode with a crystalline structure that features both electronic and ionic conductivity that can reversibly intercalate lithium ions with minimal structural change. Present research is reaching the theoretical energy density limits of these positive electrodes and leaves no room for satisfying our needs in electric/plug-in hybrid vehicles. Higher limits must be introduced, which potentially can be realized through redox driven phase-transformation chemistry that involves sulfur or oxygen as positive electrodes. These future generation systems offer increased energy densities, reduced cost factors and more benign environmental factors due to their use of non-toxic elements.

Sulfur is a promising positive electrode for lithium batteries because its chemistry is vastly different from that which governs typical intercalation materials (i.e. $LiFePO_4$, $LiMn_2O_4$) - 2 electron *vs*. 1 electron transfer, low *vs*. high molecular weight. In its most stable form, sulfur forms a molecular structure with a density of 2.07 g cm^{-3} comprised of stacked eight atom rings (S_8). In typical lithium sulfur (Li-S) cells (**Figure 1.1a**), lithium

metal is used as the negative electrode and is separated from the positive sulfur electrode by an ion conducting liquid or solid electrolyte. During discharge of the cell the sulfur-sulfur bonds are cleaved and the S_8 ring is opened and subsequent shortening of the sulfur chain length is thought to occur as shown in **Figure 1.1b**. The overall redox couple of a Li-S cell is described by the reaction, $S_8 + 16Li \leftrightarrow 8Li_2S$ and occurs at a potential of 2.15 V vs. Li/Li^+ which is ~2/3 lower than typical intercalation transition metal oxide electrode materials. This lower potential is not detrimental for practical applications because the gravimetric capacity of sulfur is the highest of any solid positive electrode material, at 1675 mA h g^{-1}_{sulfur}. It correlates to theoretical energy densities of 2500 Wh kg^{-1}_{sulfur} or 2800 Wh L^{-1}_{sulfur} based on weight or volume respectively.[1] This affords the Li-S cell up to 5 times greater energy densities when compared to conventional lithium-ion batteries at a significantly lower cost.

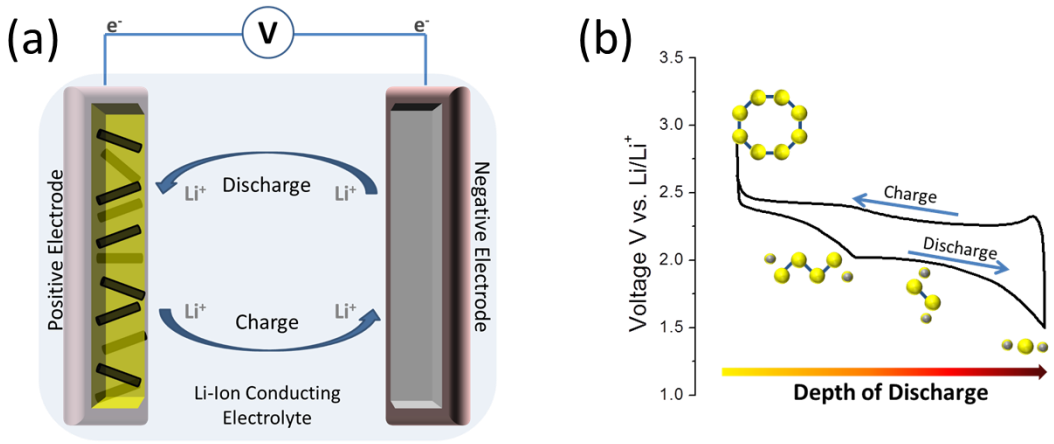

Figure 1.1 a) Schematic illustration of a typical Li-S cell. The positive electrode consists of sulfur (yellow) and a conductive additive (black, ex. carbon) separated from the negative electrode lithium (grey) by an ion-conducting electrolyte. Lithium ions propagate through the electrolyte during charge and discharge and the electrons travel through an external circuit. b) A typical voltage vs. capacity plot for a Li-S cell. During discharge sulfur, S_8 (yellow ring) is reduced by lithium (grey sphere) and the sulfur ring is opened and shortened until the final discharge product Li_2S is formed.

1.1 Challenges of a Sulfur Cathode

The significant advantages of sulfur as a positive electrode are evident, but wide-scale commercial use is so far limited because of some key challenges that must be addressed. The first main issue is that sulfur is both ionically and electrically insulating.[2] The insoluble low order lithium polysulfide discharge products are also expected to be electronic insulators, although their properties are uncertain as they have not been isolated as single phases. To overcome the insulating nature of these materials, intimate contact of conductive additives such as carbon or metals with high surface areas (i.e. nano-sizing)

augment the electrical conductivity, and organic electrolytes that wet the sulfur create pathways for ionic transport. Through reducing the sulfur particle size, the diffusion path for electrons and lithium ions is greatly reduced and leads to a higher utilization of the active sulfur mass.

These are not the only challenges in the Li-S cell. Most of the problems arise because of the intermediate discharge products (Li_2S_x, $2 < x < 8$). Upon reduction by lithium in an organic electrolyte, sulfur is reduced stepwise to a sequence of highly soluble lithium polysulfide intermediates. These intermediates can diffuse through the electrolyte to the lithium metal negative electrode where they are reduced further to insoluble Li_2S_2/Li_2S which can form dendrites and reduce the active lithium surface area.[3,4] Once this insulating layer is formed on lithium, subsequent higher order polysulfides (S_n) present in the electrolyte can become reduced at this surface to lower order polysulfides (S_{n-x}). S_{n-x} ions can diffuse back to the positive electrode where they are re-oxidized to S_n. The diffusion of lithium polysulfides between the electrodes is termed the "sulfur shuttle mechanism" and is a major cause of active mass loss, low Coulombic efficiency (excess energy required to charge the cell than obtained from discharge of the cell) and self-discharge (discharge of the cell when no load is applied) in a Li-S cell. The last main issue with the Li-S cell are the low order insoluble final discharge products Li_2S_2/Li_2S. These can form on the exterior of the electrically conducting host that is mixed with sulfur and build-up over many cycles to form highly insulating agglomerates that increase impedance and cause active mass loss.[5,6]

2. Contained Cathodes:

2.1 Macro/Meso/Microporous Carbon

In order to effectively house sulfur, the host must contain the sulfur without significantly diminishing the overall practical properties of the cell, i.e. the gravimetric/volumetric energy density. The optimal material to satisfy these conditions is lightweight, conductive and can "wire-up" the insulating sulfur, such as one made predominately of carbon. This configuration was used in the earliest reports, but it failed to harness the potential of carbons to limit polysulfide dissolution by trapping sulfur and its reduced species at the positive electrode owing to primitive carbon architecture.

Carbon is highly effective as an electronic conduit to enable redox accessibility of the sulfur but it can also act as a framework to encapsulate the redox products. A straightforward solution is to introduce pores in the carbon that sulfur can impregnate. Pore size is defined by the IUPAC as being macro (> 50 nm), meso (2 – 50 nm) or micro (< 2nm). Various carbons embodying these pore structures and their combinations have been employed recently with varying degrees of effectiveness.

Macroporous carbons have been the least utilized for Li-S cells owing to their open architecture which is highly ineffectual at containing soluble polysulfides. However, if the macroporous carbon is coupled to a high viscosity electrolyte, the lithium polysulfides are limited in mobility and will predominately remain at the positive electrode. Watanabe *et al.* used an ordered inverse opal carbon to house sulfur and replaced the commonly used low viscosity organic electrolytes with a high viscosity glyme-Li salt.[7] This electrolyte is similar to a room temperature ionic liquid in that it consists purely of $[Li(glyme)]^+$ cations and $TFSI^-$ anions. It afforded relatively stable cell cycling with a reversible capacity of

over 700 mA h g^{-1}_{sulfur} after 50 cycles and a Coulombic efficiency of 97%. While the results are promising, the current density was low (139 mA g^{-1}_{sulfur}) and the poor scalability of inverse opal carbons is problematic for large-scale applications.

Most of the recent reported research on porous carbon positive electrodes has focused on mesoporous carbons (MC's), following on early work by the Nazar group where small carbon mesopores (3-4 nm) and a hydrophilic polymer coating provided effective confinement of sulfur and its reduction products to yield high reversible capacities up to 1320 mA h g^{-1}_{sulfur}.[8] A question concerns what pore size and distribution are optimal. Liu *et al.* have used a systematic approach to determine the effect that both pore size and sulfur loading have on the cycling stability and overall capacity of the Li-S cell.[9] A series of MC's with tunable pore sizes (3, 7, 12 and 22 nm) and pore volumes up to ~4.8 cm^3 g^{-1} were synthesized using a hard template approach. The sulfur was infiltrated into the various MC's at different weight ratios using a two-step infiltration technique. Sulfur dissolved in carbon disulfide was mixed with the MC and once dry, the composite was heated at 155 °C where the low sulfur viscosity permits flow into the carbon pores. The weight fraction of sulfur gradually increased as the pore size of the MC increased, and a sulfur content of 83 wt% was reported for the 22 nm MC material. Surprisingly, all of the sulfur/carbon composites exhibited almost identical initial sulfur utilization even though the weight ratio of sulfur was significantly different (56 wt% to 84 wt%) between MC's. Contrary to other reports, this suggests there is no influence on the battery performance even if the MC is fully "stuffed" with sulfur. The MC with the largest pore size/volume clearly should be used to optimize both gravimetric and volumetric capacities were this to be the case.

Another method of sulfur entrapment is to utilize a bimodal MC as the sulfur host. The first demonstration of this concept by Dudney *et al*. used a hierarchically structured sulfur-carbon nanocomposite material as the high surface-area positive electrode.[10] A porous carbon with a uniform distribution of mesopores of 7.3 nm was synthesized through a soft-template synthesis method, followed by KOH activation to result in a bimodal porous carbon with added microporosity of less than 2 nm to the existing mesopores while maintaining integrity of the original carbon. More recent work has created bimodal carbons using a double template approach to directly fabricate highly ordered carbons with pore size split between ~6 nm and ~2 nm pores.[11,12] Each pore contributes an equal amount of pore volume with the smaller pores existing in the walls of the larger ones. When sulfur was impregnated into the carbon host, the smaller pores preferentially filled first (**Figure 1.2a**). This optimized the use of the smaller super-micropores to entrap the sulfur while the larger pores facilitated electrolyte ingress throughout the structure. An improvement on this concept was demonstrated by creating spherical bimodal-carbon particles around 300 nm in dimension with the same pore distribution (**Figure 1.2b**). Nazar *et al.* were able to cycle these sulfur/carbon electrodes at a high current rate of 1C and maintain a high and relatively stable discharge capacity of 850 mA h g^{-1}_{sulfur} at the 100^{th} cycle (**Figure 1.2c**).[13]

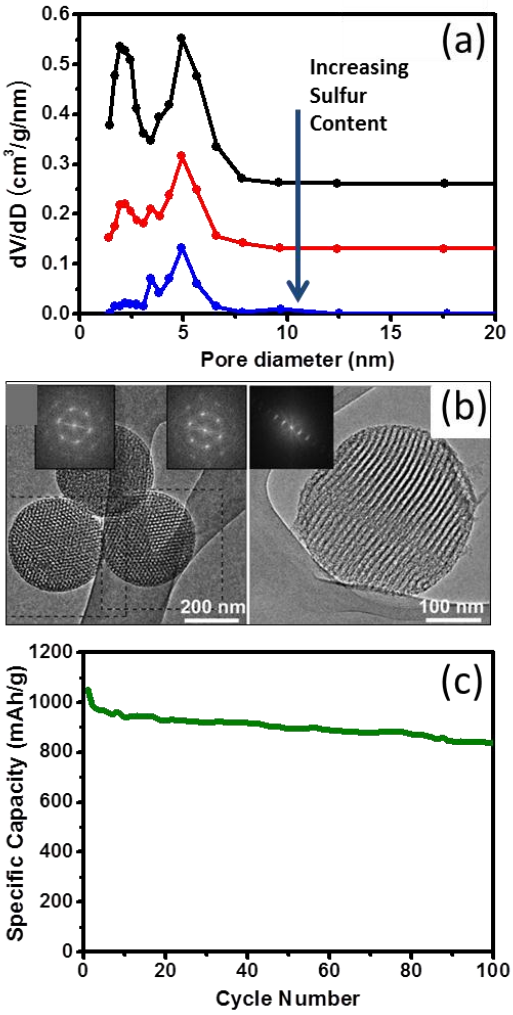

Figure 1.2 a) Pore size distribution of the bimodal mesoporous carbon (BMC) with different sulfur loadings.[11] b) TEM micrographs of spherical BMC nanoparticles showing the 2-D hexagonal structure.[13] c) Cycling performance of BMC nanoparticles with 70 wt% sulfur at a 1C rate.[13]

Another approach similar to creating a bimodal pore structure has been achieved by Archer *et al.* with the synthesis of hollow carbon spheres that exhibit a porous outer shell with small 3 nm pores and a large interior cavity around ~200 nm.[14] While this may not be considered bimodal in most respects, it effectively creates an enclosed area where

the sulfur can be stored and polysulfides have difficulty diffusing out because of the small pores in the carbon shell. The hollow carbon spheres were reported to hold 70 wt% sulfur and they retained 91% of their initial capacity (1071 mA h g^{-1}_{sulfur}) after 100 cycles at a moderate C/5 rate. Possible drawbacks to the hollow carbon spheres are the fragility of the porous carbon shell and scalability of the process. A vapour infusion method is required for sulfur impregnation involving three separate passes to obtain a high sulfur loading.

Microporous carbons have also been used as hosts for sulfur in Li-S cells. Gao *et al.* used sucrose as a carbon precursor to form microporous carbon spheres with a very narrow pore size distribution of less than 1 nm.[15] Their material exhibited highly stable cycling with 42 wt% sulfur loading and high capacity above 900 mA h g^{-1}_{sulfur}. However, an increase in sulfur content to just 51 wt% dramatically decreases the discharge capacity by ~600 mA h g^{-1}_{sulfur}. The material also exhibited an unusual discharge profile that did not have the characteristic two voltage plateau evident in most other Li-S reports. This may be due to reaction of the carbon with sulfur to form a bonded carbon-sulfur composite owing to heat treatment, or the alkyl carbonate electrolyte mixture chosen for this work. Recent studies performed by Abruña *et al.* show that carbonate based solvents undergo side reactions in the presence of nucleophilic sulfide anions.[16] Activated carbon (AC) (in the form of fibres woven into a cloth) has also been examined by Aurbach *et al*., as a microporous host for sulfur that, uniquely, does not require binder.[17] An inexpensive commercial AC cloth with high surface area (2000 m^2 g^{-1}) and narrow pore size distribution (< 2 nm) was impregnated with 33 wt% sulfur and cycled at an intermediate current density of 150 mA g^{-1}_{sulfur}. A large, stable discharge capacity of 1057 mA h g^{-1}_{sulfur} was obtained with a very high Coulombic efficiency. The latter is aided by the use of

$LiNO_3$ in the electrolyte to passivate the negative electrode and limit the sulfur shuttle mechanism.

2.2 Graphene

It was only a matter of time before arguably the most popular material of the past decade was coupled to sulfur in a Li-S battery. Graphene's advantageous properties of very high conductivity, large surface area and the ability to tune the hydrophobicity/philicity with surface functionalization has led to a few different methods of marrying it with sulfur to make effective electrodes.[18,19,20,21,22,23] Two different designs for sulfur/graphene composites have been employed with each having its positive characteristics. The first method utilizes large sulfur particles enveloped by graphene/graphene oxide sheets - with either a polymer layer buffering the sulfur[19], or with the sulfur particles simply in intimate contact with the graphene[21,22]. The sulfur particles grown with a polymer coating followed by a graphene layer showed an ability to be cycled over 140 cycles at a C/2 rate while maintaining a discharge capacity above 500 mA h g^{-1}_{sulfur} (**Figure 1.3a**).[19] A similar procedure was used to form a graphene oxide/sulfur composite with a final heat treatment step to melt sulfur into the 3D disordered graphene oxide (GO) sheets.[21] This composite exhibited extremely stable cycling using an ionic liquid/poly(ethylene glycol) dimethyl ether (PEGDME) electrolyte at C/10 rate with a reversible capacity of 950 mA h g^{-1}_{sulfur} over 50 cycles (**Figure 1.3b**).

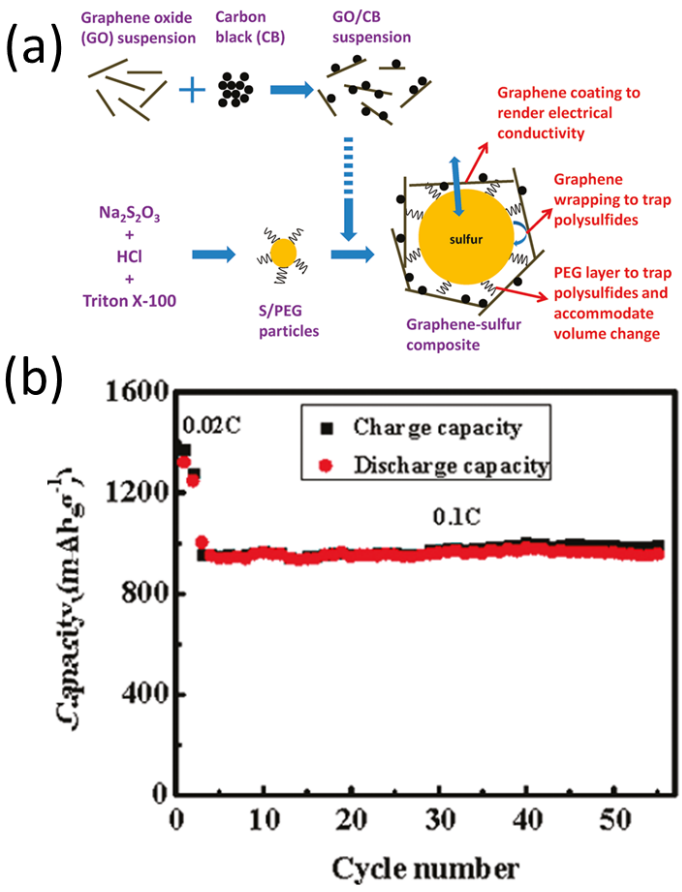

Figure 1.3 a) Schematic illustration of the synthesis process to form graphene/polymer coated sulfur particles.[19] b) Cycling performance of a graphene oxide/sulfur composite using an ionic liquid/PEGDME electrolyte at 0.1C rate.[21]

Another approach to combine sulfur and graphene is to sandwich sulfur particles between functionalized graphene sheets and apply a Nafion™ coating. This is proposed to significantly limit sulfur loss from the positive electrode owing to repulsive interactions of the Nafion SO_3^- moieties with the polysulfide anions that restrict diffusion into the electrolyte.[20] Thermally expanded graphite oxide is also effective as a 3D network; we note that 60 wt% sulfur that is melt-infiltrated exhibits a high initial discharge capacity of 1210 mA h g^{-1}_{sulfur} and maintains 73% capacity retention over 70 cycles at a current

density of 280 mA g^{-1}_{sulfur}.[23] Graphene and graphene oxide are very promising hosts for sulfur because of the wide range of compositions that can be produced through functional chemistry as well as the different architectures that can be constructed around sulfur particles or melt-diffused sulfur to form sandwiched/interleaved composites.

2.3 Carbon Nanotubes/Fibers

Multi-walled carbon nanotubes (MWCNT) in a Li-S cell have long been investigated as a highly conductive form of carbon that might provide an encapsulation effect for sulfur due to their 1D porous structure. Jin *et al.* used a precipitation technique to infiltrate sulfur into the large pore of MWCNT's by oxidation of sodium polysulfide species in the presence of MWCNT's.[24] The composite exhibited high initial sulfur utilization but had fairly rapid capacity fading over thirty cycles with only 63% capacity retention. This suggests that MWCNT's have a very limited effect at retaining soluble polysulfides. Limitations occur because of their 1D structure and a typical length on the order of a few microns which limits Li-ion diffusion compared to a more open 3D network. However, recent work that features a new method of infiltrating sulfur into disordered carbon nanotubes (DCNT's) holds promise. Wang *et al.* formed DCNT's from polyaniline deposited in an anodized alumina membrane (AAO).[25] The sulfur was incorporated into the DCNT's through a vapour infusion method whereby smaller sulfur molecules (S_2) could theoretically penetrate further into the carbon structure and possibly even penetrate graphitic layers. Various impregnation temperatures under vacuum were attempted, with 500 °C proving optimum for stable cycling and providing composites with 40 wt% sulfur active mass. Several hurdles remain as there is a significant irreversible capacity in the first few cycles which is due to excess sulfur on the surface of the DCNT's.

Carbon nanofibers (CNF's) have also been investigated as conductive additives[26] to carbon/sulfur composites, or more importantly utilized in a similar fashion to the DCNT's discussed previously. Zhang *et al.* used porous CNF's synthesized by electrospinning a polyacrylonitrile/polymethyl methacrylate mixture followed by carbonization to remove polymethyl methacrylate and create pores in the fiber walls.[27] Sulfur was introduced by precipitation from aqueous solution with further heat treatment at 155 °C and 160 °C to infiltrate sulfur and remove any excess that is present on the surface. At low rates (0.05C), using a viscous electrolyte comprised of an ionic liquid (N-butyl-N-methylpyridinium TFSI) and PEGDME, the CNF/sulfur composite (42 wt% sulfur) exhibited an initial discharge capacity of nearly 1400 mA h g^{-1}_{sulfur} and retained 82% capacity after 30 cycles.

CNF networks have also been synthesized through a templating method using an AAO membrane similar to the previous DCNT's.[28] The premise for the study was to obtain a material with sulfur residing only in the interior of the fibers so that polysulfide diffusion was limited to the ends of the fibers. This was accomplished by coating the cylindrical pores of an AAO membrane with carbonized polystyrene and subsequently infiltrating the carbon pores with sulfur. The AAO template was removed with phosphoric acid, which left CNF's with only sulfur in the interior. Upon cycling the material in a low viscosity organic electrolyte it showed signs of polysulfide dissolution, with an ~ 50% capacity fade over 150 cycles at a C/5 rate, although a specific capacity of about 730 mA h g^{-1}_{sulfur} was still retained. Active mass loss may be attributable to the less than ideal sulfur confinement with such large pore substrates, but architectural improvements will undoubtedly be forthcoming soon.

2.4 Tubular Porous Polymers

Porous polymers have also been researched as hosts for sulfur which mimic the structure of carbon nanotubes/fibers.[29,30,31] Liu *et al.* have performed interesting studies using polyaniline nanotubes to host sulfur both in its elemental form and as part of the polymer backbone.[32] Sulfur was reacted with polyaniline nanotubes at 280 °C in order to chemically incorporate sulfur carbon bonds in the polymer through an i*n situ* vulcanization as shown in **Figure 1.4**. Elemental sulfur was still present in the sample (62 wt%) and was postulated to be present in the pores of the polymer structure. The composite exhibited an initial capacity of 755 mA h g^{-1}_{sulfur} at a C/10 rate but the capacity increased in the next few cycles before suffering a slight capacity fade to 837 mA h g^{-1}_{sulfur} after 100 cycles. The increase in capacity was reasoned to be due to low surface area of the composite that initially did not allow electrolyte to penetrate the full structure. Upon cycling, some of the sulfur is reduced to soluble polysulfides so the additional porosity allows for higher accessibility and capacity. The capacity fading may be due to degradation of the polymer-sulfur backbone as the disulfide bonds in the polymer may not reform upon oxidation.

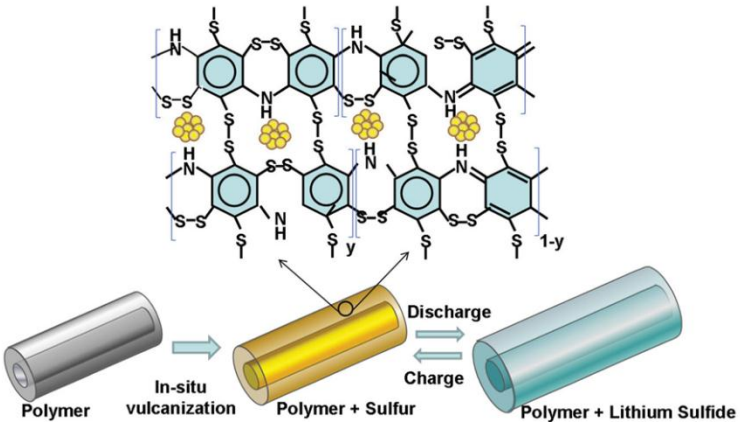

Figure 1.4 Schematic illustration of the construction and discharge/charge process of the polyacrylonitrile nanotube/sulfur composite.[32]

MWCNT's have also been used as a support to create a porous polyacrylonitrile/sulfur composite.[33] Polyacrylonitrile was coated on the exterior surface of MWCNT's and the material was treated with varying amounts of sulfur (30, 48 and 63 wt%). The best overall results were obtained for the 48 wt% sulfur composite, which exhibited 85% capacity retention, amounting to ~590 mA h g^{-1}_{sulfur} after 50 cycles at a C/10 rate. The composite has good rate capabilities and is able to be discharged up to 4C while maintaining a discharge capacity above 400 mA h g^{-1}_{sulfur}, but the average discharge voltage is low at 1.8 V and when coupled to the marginal capacity, significantly hinders the gravimetric energy density of the material.

2.5 Porous Metal Oxides

Carbonaceous materials are not the only hosts for sulfur that have been researched in the past few years for the Li-S battery. Tarascon *et al.* have taken guidance from approaches to carbon coat $LiFePO_4$ to overcome its insulating nature, by carbon coating an insulating host that serves to contain the sulfur.[34] Their work utilized an insulating metal-organic framework (MIL-100) consisting of an open framework of small mesopores (~2.5-2.9 nm) and micropores (~0.5 and ~0.9 nm). Sulfur was impregnated through the well-known melt diffusion technique,[8] affording a composite with 48 wt% sulfur. Since MIL-100 is insulating, up to 50 wt% carbon was necessary to coat the particles to ensure good electrical conductivity. The material (amounting to 24 wt% sulfur in the electrode) was compared to an electrode containing mesoporous carbon CMK-3 with similar sulfur filling (52 wt%) and 20 wt% Ketjen Black (total 42 wt% sulfur in the electrode). The MIL-100/S composites exhibited high capacity, and also more stable cycling, suggesting that the oxidic framework helps to retain polysulfide. This concept, using oxide additives, has

a similar effect to that reported by other researchers and discussed below. The drawback is the low overall capacity of the MIL-100/S after 50 cycles at C/10 (~500 mA h g^{-1}_{sulfur}) and the low sulfur content which makes the system less practical.

3. Physical Barrier Containment

The previous discussion overviewed work that focussed on providing a host for sulfur that contains the soluble polysulfides through architectural effects combined with chemical restraints. Another method of containment is to apply coatings to the sulfur host structure that physically blocks polysulfides from escaping the positive electrode, while still allowing ingress of the electrolyte to the sulfur/carbon mass.

3.1 Polymer Coatings

In the recent literature, a variety of different approaches have been utilized in order to limit polysulfide dissolution with the use of polymer coatings. Zhao *et al.* circumvented the use of a host material for sulfur and simply coated sulfur particles with a conducting polymer, polythiophene.[35] They were able to synthesize a polythiophene/sulfur composite with ~72 wt% sulfur that performed extremely well electrochemically. Using a low viscosity electrolyte of DOL:DME, the composite was cycled at a current density of 100 mA h g^{-1} and retained 74% of its initial capacity (1120 mA h g^{-1}_{sulfur}) after 80 cycles.

Cui *et al.* have used a carbon host (CMK-3), that is highly effective at retaining polysulfides itself because of its small ~3-4 nm pores[8] as a substrate to polymer coat in order to limit polysulfide dissolution even further as shown in **Figure 1.5**.[36] CMK-3/S composites were prepared and mixed with the conductive polymer PEDOT:PSS which forms a thin 10-20 nm coating. While the effect of the polymer coating on electrochemical performance was not considerable, a slight increase in capacity stability was observed over

bare CMK-3/S. The PEDOT:PSS coated CMK-3/S was able to retain an overall capacity greater than 600 mA h g^{-1}_{sulfur} after 150 cycles at a C/5 rate.

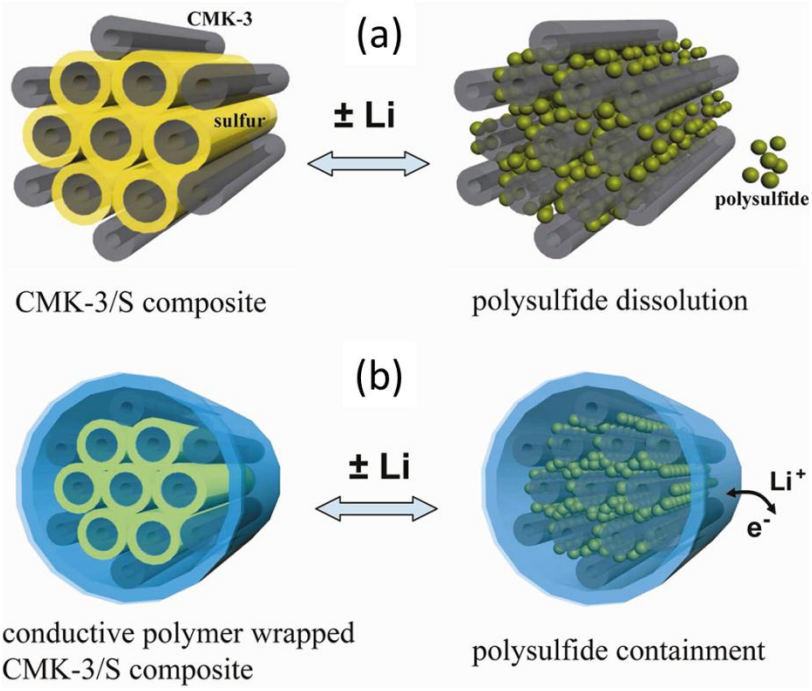

Figure 1.5 Scheme of polymer-coated CMK-3/sulfur composite for improving the positive electrode performance. (a) In bare CMK-3/S particles (gray: CMK-3, yellow: sulfur), polysulfides (green color) still diffuse out of the carbon matrix during lithiation/delithiation. (b) With conductive polymer coating layer (blue color), polysulfides could be confined within the carbon matrix. Lithium ions and electrons can move through this polymer layer.[36]

A third conducting polymer - polyaniline - has also been utilized as a coating for a MWCNT/S composite.[37] The MWCNT's were impregnated with sulfur before oxidative polymerization of polyaniline. The sulfur content remained high in the composite at 70 wt% and also retained a crystalline structure. The material showed very stable cycling over 80 cycles and not surprisingly had less capacity fade than uncoated MWCNT/S. The rate

capability of the material was also found to be quite good with ~90% capacity retention after 80 cycles at current densities ranging from 200 – 1000 mA g^{-1}_{sulfur}.

4. Additives to Retain Polysulfides

4.1 Porous Metal Oxides

Containing soluble polysulfides has been discussed through both physical and chemical barriers of the host material or coatings on the host material for sulfur. Another method of containment at the positive electrode is to provide additives in the positive electrode matrix that can attract and hold polysulfides so that they do not diffuse to the negative electrode. To employ this concept Nazar *et al.* utilized mesoporous silica as an additive to a large pore mesoporous carbon/sulfur electrode (**Figure 1.6a**).[38] The main interaction that the polysulfides have with the additive is through surface sorption and therefore the surface area is increased significantly by synthesizing the additive with a mesoporous structure. At a C/5 rate, the capacity versus a cell without additive was both increased and much more stable over 40 cycles. The silica additive was able to sorb polysulfides during intermediate discharge and release them near the end of discharge so that they could be further reduced in the mesoporous carbon with ~94% of the sulfur being reversibly sorbed in the silica at the 40^{th} cycle. The amount of sulfur present in the electrolyte after 30 cycles decreased by more than 30% compared to a cell consisting of no silica additive (**Figure 1.6b**).

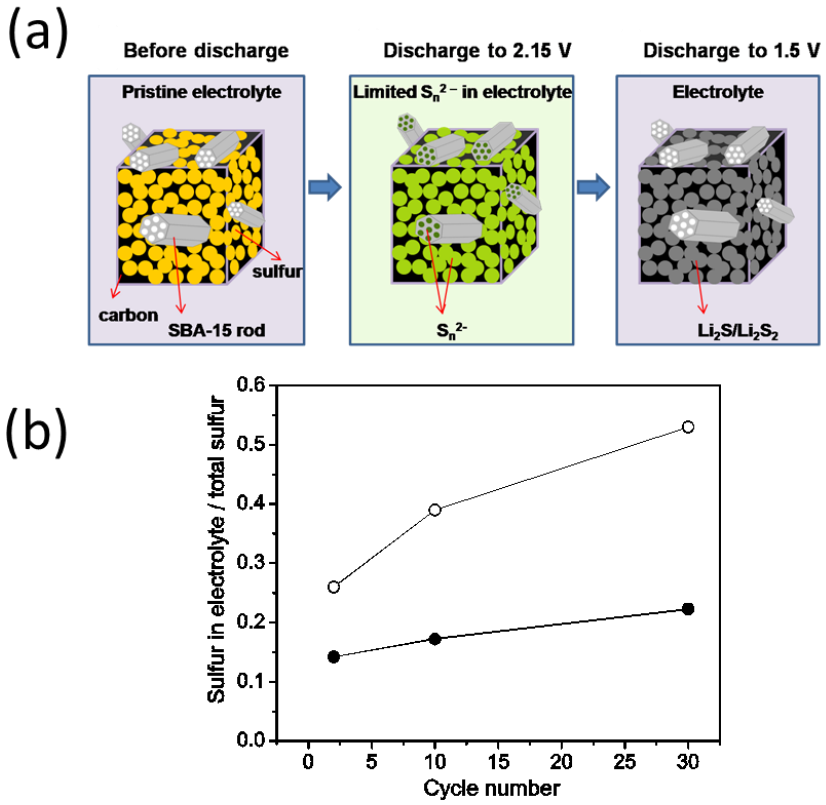

Figure 1.6 a) Schematic diagram showing the effect of SBA-15 rods in the electrode on reversibly absorbing/desorbing polysulfide anions. b) Percentage of sulfur dissolution into the electrolyte, from the SCM/S positive electrode (open dot curve) and from the SBA-15 added SCM/S positive electrode (solid dot curve).[38]

5. Summary

The prospectus of Li-S batteries has improved remarkably over the last few years, but more improvements are still needed at the positive electrode. The containment of polysulfides is critical to increase cycle life and minimize capacity fading. Achieving full, reversible reduction of Li_2S_2 to Li_2S, which accounts for half of the theoretical capacity, is vital to improving energy density. Fundamental studies are necessary to understand and control this process better. While some research is informative, a more realistic, scalable

approach to materials design is important. Tailored hosts for sulfur need to be optimized to provide high tap densities, large pore volumes for increased sulfur loading while still containing the sulfur. Commercially viable additives or coatings for positive electrodes may prove essential for operation, but they must be efficient in both weight and volume so that they do not drastically decrease the performance of the hosts for sulfur. Finally, innovations at the negative electrode are critical to reduce concerns of dendritic growth. With these considerations in mind, however, sulfur is unquestionably a viable positive electrode material and scientists are proving that with the recent research outlined here.

6. Scope of this Thesis

Chapter 1 is a general introduction of pertinent research that has been undertaken in the past few years on the Li-S battery. Reproduced with permission from S. Evers and L. F. Nazar, *Acc. Chem. Res.*, DOI: 10.1021/ar3001348, (2012). Copyright 2012 American Chemical Society. Chapter 2 is an overview of the methods and techniques that were used to analyze the various materials presented in this thesis. Chapter 3 examines a graphene-sulfur composite and its electrochemical properties in a Li-S battery. S. Evers and L. F. Nazar, *Chem. Commun.*, **48**, 1233, (2012). Reproduced by permission of The Royal Society of Chemistry. Chapter 4 examines the stabilization of a Li-S batteries capacity through the addition of a mesoporous titania. Reproduced with permission from S. Evers, T. Yim and L. F. Nazar, *J. Phys. Chem. C*, **116**, 19653, (2012). Copyright 2012 American Chemical Society. Chapter 5 examines porous carbon spheres with sulfur filled shells and their high capacity retention. Chapter 6 examines microporous carbons and their ability to retain lithium polysulfides at the positive electrode.

Chapter 2

Characterization Methods and Techniques

2.1 Powder X-ray Diffraction

Powder X-ray diffraction (PXRD) patterns were collected using a Bruker D8-Advance powder diffractometer equipped with a Vantec-1 detector, using Cu-Kα_1 radiation (λ = 1.5406 Å). The powder samples were placed on a zero background silicon plate and were scanned at various stepping rates in order to optimize the resolution and signal to noise ratio.

The basis for PXRD derives from three important discoveries at the turn of the 19th century. In 1895, X-rays were discovered by Wilhelm Röntgen[1] and in 1912 Laue *et al.* discovered that X-ray radiation could be diffracted by crystals[2]. The final discovery was made in 1913 by Sir William Bragg and is known as Bragg's Law[3]. Bragg's Law (**equation 2.1**) can explain the appearance of a diffraction pattern through interference of X-ray reflections from crystal planes in a sample.

$$n \cdot \lambda = 2 \cdot d \cdot \sin\theta \qquad (2.1)$$

Bragg's Law is schematically shown in **Figure 2.1** where θ represents the incident angle of the incoming X-ray radiation with respect to the crystallographic planes that are created by the ordering of atoms (represented as blue spheres in **Figure 2.1**) in the sample. Two parallel incident X-rays labeled (A) and (B) are diffracted by the atoms in the sample but X-ray (B) must travel $2 \cdot d \cdot \sin\theta$ further than X-ray (A) as the distance between lattice planes is defined as d. If the two diffracted X-rays are in phase and a multiple (n) of the X-

ray wavelength (λ) then the distance between crystal planes (d) can be obtained by scanning θ.

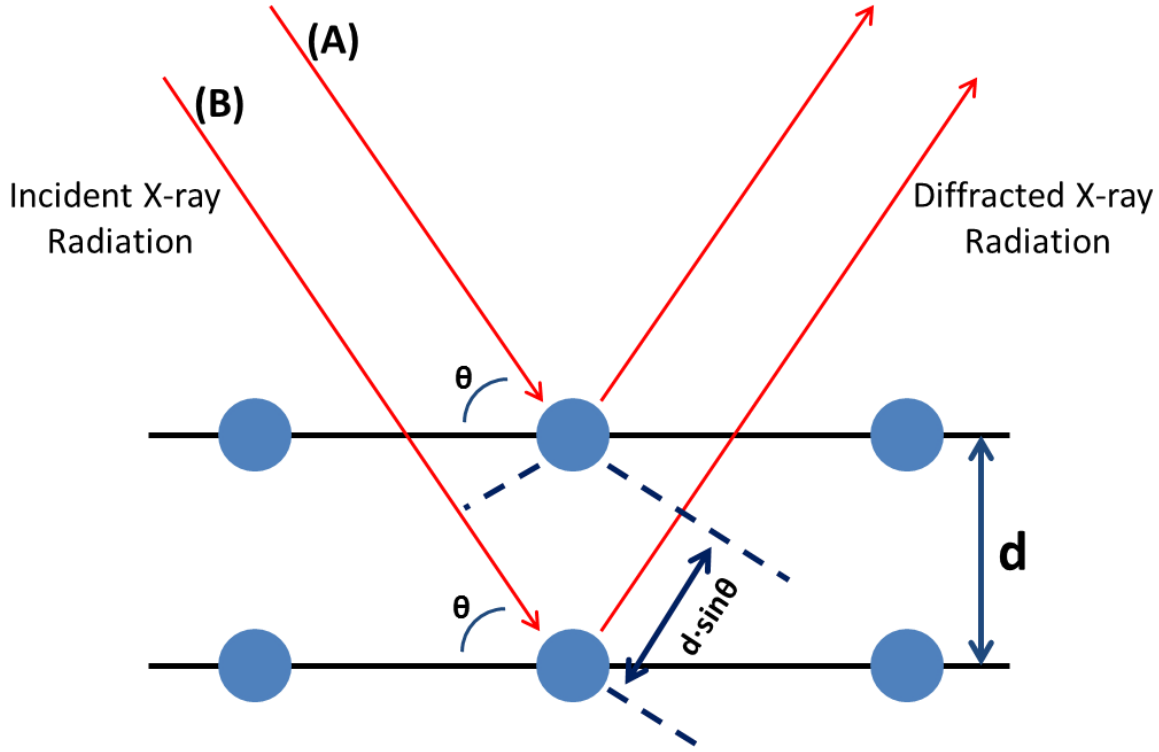

Figure 2.1 Schematic illustration of Bragg's Law.

In PXRD, X-ray radiation strikes a sample powder at a certain incident angle and since the powder is comprised of small crystals, a portion of these crystals will be oriented with their crystallographic planes at the Bragg angle θ. The sample platform is rotated with respect to the incident X-ray radiation and a pattern containing the characteristic diffractions of the sample is obtained. PXRD patterns are unique to different compounds and can be used as a fingerprint for identification of a sample.

At the nanoscale, peaks in a diffraction pattern will begin to widen as crystallite size diminishes. The Scherrer equation[4] (**equation 2.2**) relates the broadening of diffraction

lines with crystal domain size and can give a good approximation of crystallite size in the sample.

$$L = \alpha \cdot \lambda / (\beta \cdot \cos\theta) \qquad (2.2)$$

L is the coherence length of the crystal domain and β is the full width in radians at the half maximum intensity (FWHM) measured at angle θ. The wavelength λ is determined by the X-ray source and the constant α is close to unity[5].

2.2 Fourier Transform Infrared Spectroscopy and Raman Spectroscopy

Fourier transform infrared (FTIR) spectroscopy analysis was performed on a Bruker Tensor 37 spectrometer. The samples were analyzed by preparing a KBr pellet in an inert nitrogen atmosphere. Infrared radiation (IR) is passed through the sample and when the frequency of radiation is equivalent to the vibrational frequency of an atomic bond in the sample the IR radiation is absorbed. The sample is scanned over a range of IR frequencies, resulting in a plot of absorption versus IR frequencies. Only bonds between atoms that experience a dipole moment are probed.

Raman spectroscopy was performed on a LabRam HR system (HORIBA Jobin Yvon) using 633 nm laser irradiation. There are three types of Raman scattering: Stokes scattering, anti-Stokes scattering and Rayleigh scattering. Raman spectroscopy only uses inelastic scattering (Stokes and anti-Stokes) and thus Rayleigh scattering which is elastic scattering of light with a frequency equivalent to the incident radiation is not used. The three types of Raman scattering are shown schematically in **Figure 2.2**.

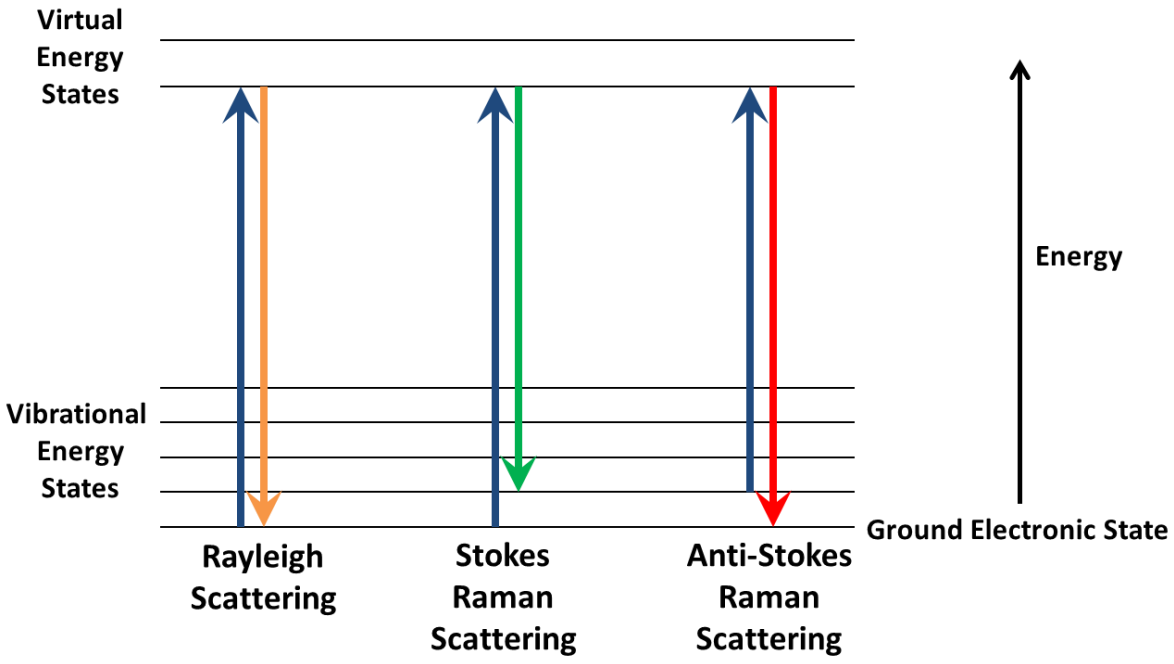

Figure 2.2 Schematic diagram of the three types of Raman scattering.

Stokes and anti-Stokes scattering are inelastic and have either less energy or more energy respectively than the incident radiation. This energy increase or decrease is directly related to and characteristic of the difference in energy between the ground electronic state and the vibrational states of a molecular bond. The anti-Stokes scattering is only seen when a molecular bond is vibrationally excited prior to irradiation and is less likely than Stokes scattering which is normally measured.

2.3 Thermogravimetric Analysis

Thermogravimetric analysis (TGA) was performed either in air or under nitrogen atmosphere on a TA Instruments SDT Q600 analyzer. TGA is used to study the thermal stability of a sample and/or its composition. In the work presented in this thesis a standard temperature program of 10 °C/min was used. A samples composition can be determined

from a measure of its weight loss as a function of temperature as long as the different components evolve at different temperatures.

2.4 Scanning Electron Microscopy

Scanning electron microscopy (SEM) was performed on a LEO 1530 field-emission SEM instrument. All samples were gold coated (~ 10 nm) to limit surface charging of the electron beam and were imaged at an accelerating voltage of 10 kV. SEM is a pivotal tool that provides information about the morphology and topography of a sample at the nanoscale. A SEM targets high energy electrons onto the surface of a sample. Secondary electrons, backscattered electrons and characteristic X-rays are then produced from the sample. In the SEM images presented in this thesis the backscattered mode of detection was used which only collects backscattered electrons. Backscattered electrons are electrons that were present in the incident beam and have been elastically scattered by the sample. High atomic number elements scatter electrons more strongly than low atomic number elements and thus appear brighter in a backscattered electron image. While backscattered electrons give less detail about morphology than secondary electrons, they can give some information about the macroscopic distribution of elements in a sample.

2.5 Scanning Transmission Electron Microscopy

Scanning transmission electron microscopy (STEM) was performed on a Hitachi HD-2000 STEM instrument. The samples were dispersed on a copper grid before imaging and were imaged at an accelerating voltage of 200 kV. A traditional transmission electron microscope focuses an electron beam onto a sample and the scattered electrons and x-rays are collected by detectors placed beneath the sample stage. In this thesis dark-field imaging or Z-contrast is used as well as bright-field imaging. In dark-field imaging high

atomic number elements appear bright in the image and low atomic number elements appear dark and vice versa for bright field imaging. The TEM configuration is used by a STEM instrument except the electron beam is moved over the sample in a raster scan. By scanning the sample with a precise narrow beam, analysis of specific predetermined parts of the sample can be obtained.

2.6 Alternating Current Impedance Spectroscopy

Alternating current (AC) impedance spectroscopy was performed on a BioLogic VMP3 instrument. The AC impedance of full cells was measured at open-circuit voltage over a frequency range of 200 kHz to 100 mHz. Impedance is a measure of the ability of a circuit to resist the flow of electrical current. In AC impedance spectroscopy, a small AC potential is applied to an electrochemical cell and the resultant current that is generated in the cell is measured. The AC potential is applied as a sinusoidal excitation and the resultant AC current signal is analyzed as a sum of sinusoidal functions. The perturbation potential applied to the cell is small so that the cells response is pseudo-linear. In this thesis, impedance data are shown in Nyquist plots. The impedance of a cell is represented mathematically as a real part and an imaginary part. The real is plotted on the x-axis and the imaginary on the y-axis. The plot consists of a series of half circles and a linear part with the high frequency perturbations on the left side of the x-axis and lower frequencies on the right. In this thesis, AC impedance spectroscopy is used as a tool to directly compare different positive electrode materials and their impedance to electrical and lithium ion conductivity.

2.7 Surface Area / Pore Volume / Pore Size Determination

Surface area, pore volume and pore size determination was performed on a Quantachrome Autosorb-1 instrument. Nitrogen adsorption and desorption isotherms were collected at -196 °C and before measurement the samples were degassed at 150 °C on a vacuum line. A nitrogen adsorption isotherm is a plot of relative pressure on the x-axis and volume of adsorbed nitrogen on the y-axis. The sample is loaded into a quartz tube and evacuated on the instrument. It is immersed in a liquid nitrogen bath at -196 °C and in incremental steps nitrogen gas is introduced into the sample tube. Nitrogen molecules adsorb on the surface of the sample and the system measures the pressure change in the sample tube compared to a balance tube. The surface area was calculated using the Brunauer-Emmett-Teller (BET) method [6]. The total pore volume was calculated from the amount of nitrogen adsorbed at a relative pressure of 0.99. The pore size distribution (PSD) was calculated using the Barrett-Joyner-Halenda (BJH) method [7] applied to the desorption branch of the nitrogen isotherm. Analysis of the carbide derived carbons in Chapter 6 required the use of a different method of analysis called Quenched Solid Density Functional Theory (QSDFT). This is required for analysis of micropores when using nitrogen as the adsorbate molecule.

2.8 Electrochemical Measurements

Electrochemical measurements involving galvanostatic cell cycling were performed on an Arbin battery cycler at room temperature. In this thesis, specific capacity, cell stability and rate capability of studied electrode materials are the primary electrochemical characteristics probed. Therefore, a galvanostatic technique is used where a constant current is applied to the cell until a predetermined cut-off voltage is reached and the

current is reversed. With this technique, single discharge/charge cycles can be analyzed in a plot of electrode capacity (x-axis) versus cell voltage (y-axis). Long-term cell cycling is probed as the cycle number (x-axis) versus specific capacity (y-axis) and from this cell stability (loss of capacity over cycles) can be analyzed. The rate capability of an electrode material refers to the ability of a material to retain capacity as the current to the cell is changed during cycling. This is a measure of the materials electronic and ionic transport properties as well as its robustness.

In this thesis, 2325 type coin cells were used to test electrode materials and their construction is shown in **Figure 2.3**. The positive electrode was prepared by mixing the electrode material being studied with a conductive carbon additive and polymer binder in a solvent and slurry-casting onto carbon-coated aluminum foil. The electrode was dried overnight at 60 °C and subsequent cell fabrication was performed in an argon filled glovebox. The electrolyte used in this thesis consists of a lithium salt dissolved in a mixed solvent with a low concentration lithium nitrate additive to protect the lithium metal negative electrode.

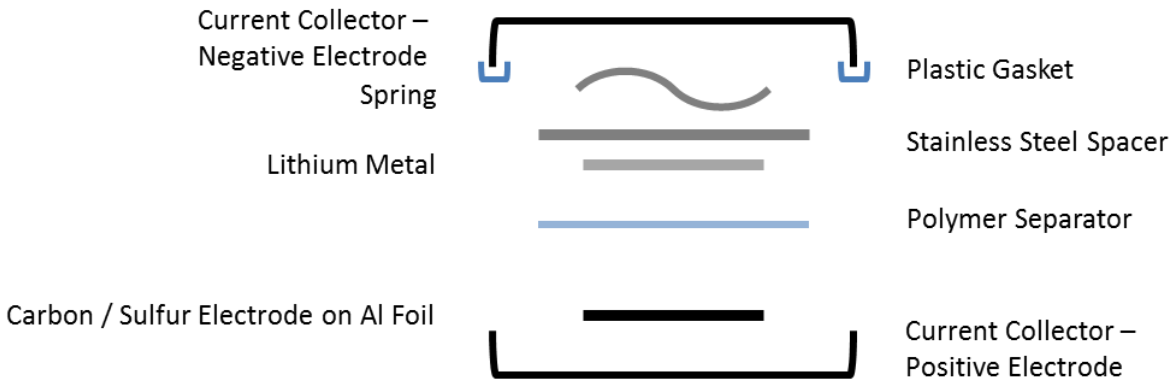

Figure 2.3 Schematic diagram of a 2325 type coin cell.

Chapter 3

Graphene-Enveloped Sulfur in a One Pot Reaction: A Positive Electrode with Good Coulombic Efficiency and High Practical Sulfur Content

3.1 Introduction

Graphene is a viable carbon matrix material for the Li-S cell since it is highly conductive and can envelope sulfur to hinder polysulfide dissolution. Previous work has shown that graphene can be used as a conductive support for polymer wrapped sulfur particles[1], melt-infiltrated sulfur[2] and interstitial sulfur particles[3]. While these materials are promising, they do not address the issue of large-scale technology for commercial applications and practical sulfur loading. This is a challenge. In general, the lower the sulfur content, the higher the sulfur capacity owing to factors such as electrolyte accessibility within the porous carbon, and electronic contact. Many papers focus on cells that exhibit very high capacity per gram of sulfur, but which contain sulfur contents well below 50% which greatly reduces their overall energy density per gram of positive electrode. Herein, a highly scalable graphene-sulfur composite (GSC) positive electrode material that exhibits the highest sulfur loading level (87 wt%) is reported. Reduced graphene oxide (rGO) is used to envelope micron sized sulfur particles, to form a highly conductive network around the sulfur particles and trap the polysulfides through favourable hydrophilic-hydrophilic interactions. Larger sulfur particles with a lower surface area to volume ratio are more advantageous than nano-sized particles because they reduce the amount of rGO required to fully envelope the particles.

3.2 Experimental

3.2.1 Preparation of graphene-sulfur composite

The synthesis of the graphene-sulfur composite (GSC) was easily accomplished by combining a mixture of graphite oxide[4] and soluble polysulfide ($Na_2S_{\sim 2.4}$),[5] and carrying out oxidation in-situ as a one pot reaction as described in **Figure 3.1**. In a typical procedure, graphite oxide (100 mg) prepared by the modified Hummer's method[4] was sonicated in 20 mL of 5mM NaOH for 1 hour to form a suspension of graphene oxide. In a separate container, sulfur (99.5% Alfa Aesar, 500 mg) was mixed with sodium sulfide nonahydrate (99.99+% Aldrich, 1g) in 100 mL 10% NaOH solution at 60°C to form a deep orange solution. The graphene oxide suspension and the sodium polysulfide solution were then mixed together and stirred for 4 hours, and a stoichiometric amount of 5% HCl solution was added to lower the pH to 2. The GSC composite was obtained after filtration and drying.

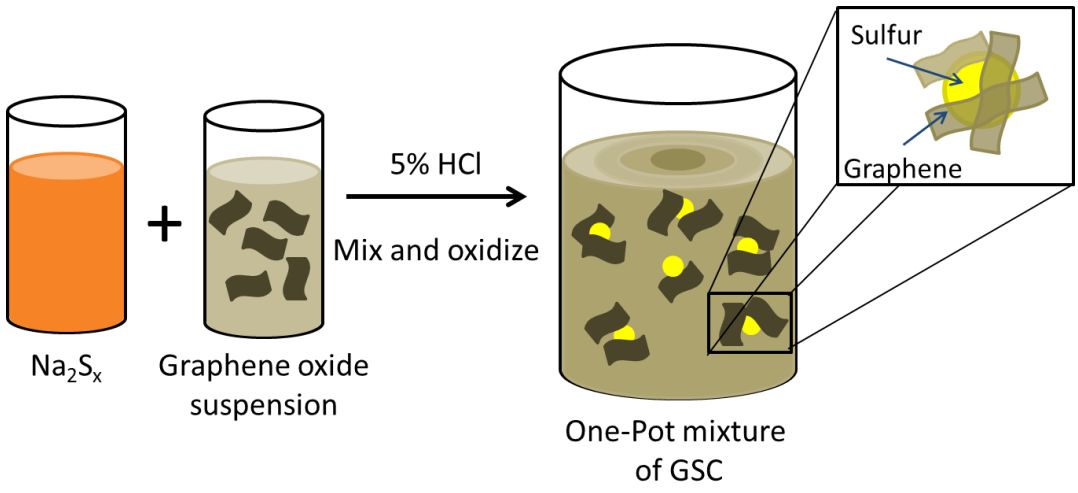

Figure 3.1 An illustration of the one-pot synthetic technique for the production of GSC.

3.2.2 Alternating current impedance spectroscopy and electrochemical analysis

The full cell impedance was performed at open-circuit voltage using a BioLogic VMP3 instrument. The AC impedance was measured over a frequency range of 200 kHz to 100 mHz. Two full cells were studied: one contained the GSC composite as the positive electrode and the other contained graphite oxide synthesized by the modified Hummer's method as the positive electrode. Both cells contained the same electrolyte as was used in the cycling studies and were made against a lithium negative electrode. The equivalent electrical circuit used to fit the data is shown in **Figure 3.2**. R_b is the bulk resistance in the cell (main contribution from electrolyte); R_s and C_s are the resistance and capacitance of the interface layer formed on the surface of the electrodes; R_{ct} and C_{dl} are the faradic charge transfer resistance and its relative double-layer capacitance; W is the Warburg impedance.

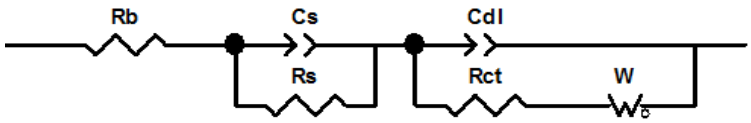

Figure 3.2 Equivalent electrical circuit used to fit the AC impedance data.[6]

Positive electrodes were prepared from GSC (90 wt%), and polyvinylidene fluoride binder (PVdF) binder (10 wt%). The positive electrode material contained 78 wt% sulfur active mass. The positive electrode material was well dispersed in cyclopentanone by agitation and sonication, and was slurry-cast onto a carbon coated aluminum current collector (Exopack Advanced Coatings). The positive electrode was tested in 2325 coin cells using an electrolyte comprised of 1M LiTFSI in a mixed solvent of 1,3-dioxolane (DOL) and tetraethyleneglycol dimethyl ether (TEGDME) (1:1 volume ratio) with 2 wt%

$LiNO_3$ additive. Lithium metal foil was used as the counter electrode. A typical cell contained a positive electrode loading of approximately 1.2 mg of sulfur. The batteries were cycled between 1.5 and 3 V using an Arbin battery cycler at room temperature. The discharge/charge rate C/5 (334 mA h g^{-1}_{sulfur}) corresponds to a current density of 0.4 mA cm^{-2}.

3.3 Results and discussion

3.3.1 Powder X-ray diffraction and alternating current impedance measurements

The PXRD patterns of graphite, graphite oxide, sulfur and GSC are shown in **Figure 3.3**. The graphite starting material is clearly oxidized by the modified Hummer's method[4]: the d-spacing increases from 3.35 Å for natural graphite to 8.42 Å for the graphite oxide which is in good agreement with previously reported data for graphite oxide.[7] The synthesis relies on the in-situ oxidation of the polysulfides with acid in the presence of the exfoliated graphene oxide, which simultaneously forms the sulfur particles and wraps them with the conductive agent. On fabrication of the GSC, a characteristic sulfur PXRD pattern is obtained. It is noteworthy that no graphite or graphite oxide peaks appear in the GSC pattern which proves that the reduced graphene oxide sheets are in a substantially exfoliated state and do not restack upon the oxidation of sulfur in the synthesis. The one-pot synthesis of GSC also aids in the intimate contact between the sulfur particles and the rGO sheets, and provides synthetic synergy. When the two solutions are initially mixed before HCl oxidation, the strongly basic sodium polysulfides can undergo a redox reaction with the rGO to form a slightly more graphitic carbon. A decrease in resistance of the GSC electrode compared to pure graphite oxide is shown by AC impedance spectroscopy (**Figure 3.4**). The polysulfides will be slightly oxidized on

the rGO surface and this can form nucleation sites for further sulfur particle growth by HCl oxidation of the remaining sodium polysulfides in solution.

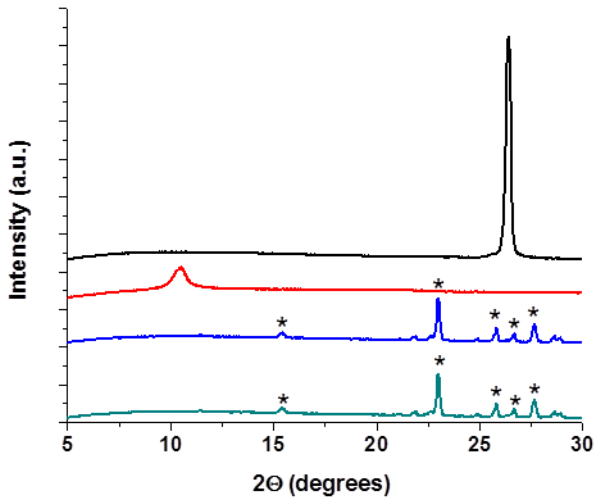

Figure 3.3 PXRD of graphite (black), graphite oxide (red), sulfur (blue), and graphene-sulfur composite (GSC) (green) (* represents characteristic sulfur peaks).

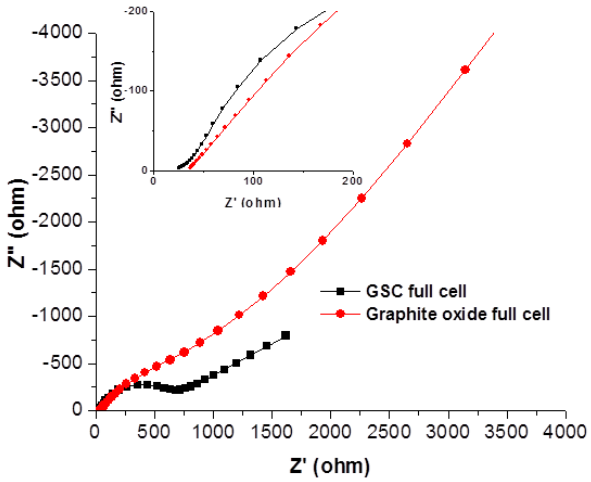

Figure 3.4 The AC impedance Nyquist plot of the GSC composite full cell (black) and the graphite oxide full cell (red), inset: zoom-in of high frequency region of impedance plot.

3.3.2 Raman spectroscopy measurements

The nature of the carbon and sulfur in the GSC composite was analyzed by Raman spectroscopy and the spectrum is shown in **Figure 3.5**. The sulfur particles exhibit a characteristic peak at ~ 520 cm^{-1} which is due to the A1 symmetry mode of the sulfur-sulfur bond.[8] The relative intensity of the D peak at ~1350 cm^{-1} which represents disordered carbon and the G peak at ~1590 cm^{-1} which represents graphitic carbon are indicative of the degree of graphitization of a carbon sample.[9] The intensity ratio of the D and G peaks is $I_D / I_G = 1.22$. This means that the average distance between defects is < 4 nm in the graphene that envelops the sulfur.[10] The rGO sheets that envelope the sulfur particles in GSC therefore have both disordered and graphitic domains as expected from the synthesis method. High temperatures and strong reducing conditions are necessary to reduce graphene oxide to "graphene", which are incompatible with the sulfur moitié in the composite.

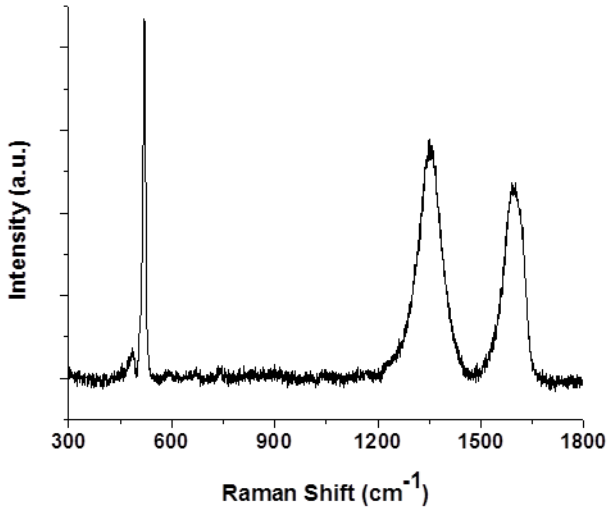

Figure 3.5 Raman spectrum of GSC with its characteristic sulfur peak at ~520 cm^{-1}, and the D band (~1350 cm^{-1}) and G band (~1590 cm^{-1}) that are characteristic of graphene.

3.3.3 Scanning electron microscopy, transmission electron microscopy and thermogravimetric analysis

The effectiveness of rGO as a well dispersed, flexible conductive agent is evident from the scanning electron micrographs in **Figure 3.6a** and **3.6b**, where the sulfur particles are highlighted by red squares. Sulfur is present as large micron sized particles that are completely enfolded by sheets of rGO without the use of polymers or additives. The well-known strong binding of sulfur and carbon aids in driving this interaction. The STEM image in **Figure 3.6c** clearly shows a sulfur particle that is approximately 1.5 μm in size enfolded by sheets of rGO. The carbon and sulfur elemental mapping demonstrates that sulfur is present as discrete particles embedded in the carbon tissue matrix, unlike other methods of synthesis that rely on melting of the sulfur into the graphene framework.[2]

Although that approach is viable (in principle), only a 22 wt% sulfur content was reported. The one-pot method also differs from other reports that utilized polyethylene glycol as an interface between the sulfur particles and the graphene wrap, where composites containing 50-60 wt% sulfur were obtained in a two-step process.[1] Through the in-situ one pot approach described here, a reduction in the amount of rGO required to envelope the sulfur is achieved. The sulfur content, measured by thermogravimetric analysis (**Figure 3.7**) was 87 wt%. This greatly increases the overall gravimetric capacity of the material with respect to total mass of positive electrode, especially as no additional carbon was used to prepare the positive electrode.

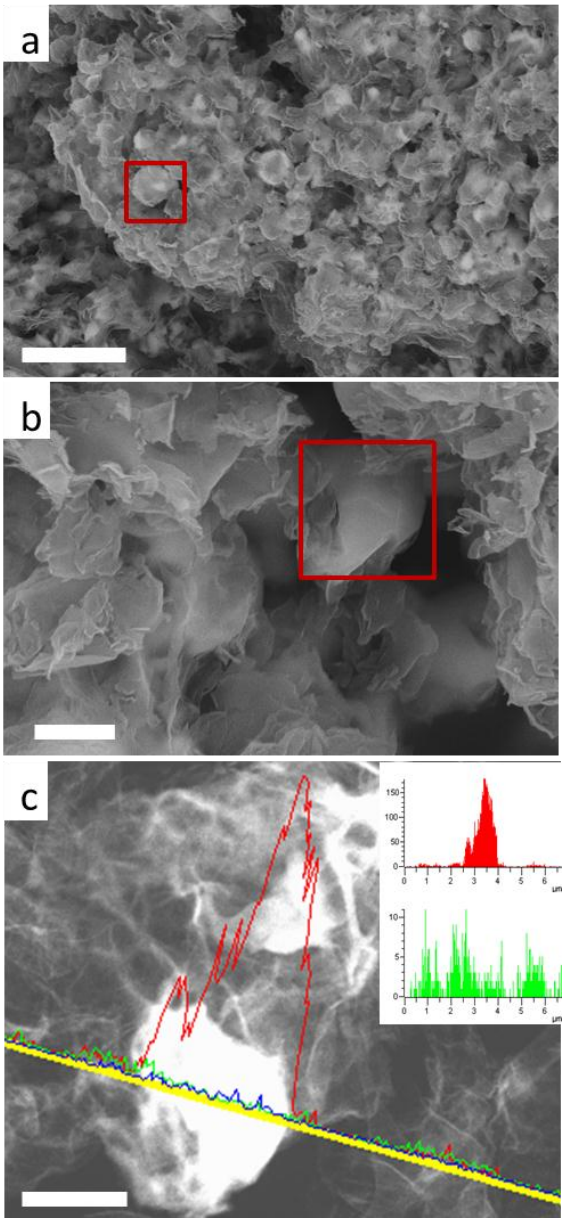

Figure 3.6 Scanning electron microscope (SEM) images of graphene-sulfur composite (GSC) (a) low magnification (scale bar = 6 µm); (b) high magnification (scale bar = 1 µm). Red squares highlight sulfur particles enveloped by rGO sheets; (c) Scanning transmission electron microscope image (STEM) of GSC and a line scan electron dispersive spectrum with plots of signal intensity as a function of distance across the specimen for sulfur (red) and carbon (green) (scale bar = 1 µm).

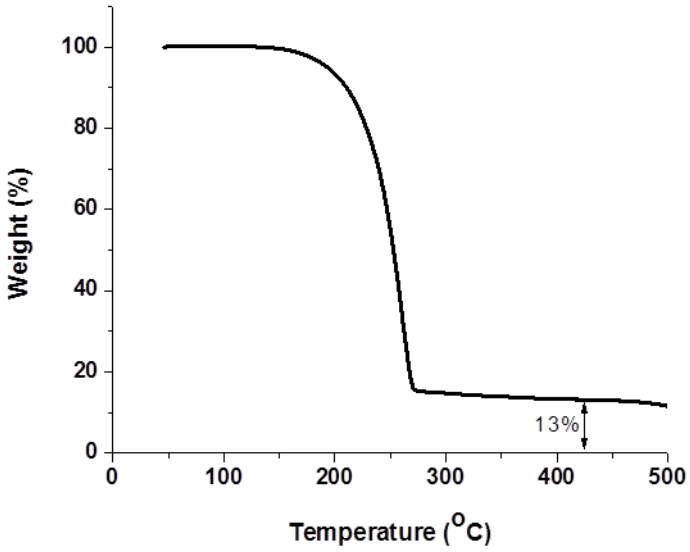

Figure 3.7 TGA curve (N_2 atmosphere) of the graphene-sulfur composite prepared as described in the experimental, showing weight loss of 87% corresponding to the loss of sulfur.

3.3.4 Electrochemical study of graphene sulfur composite

The electrochemical properties of the GSC positive electrode were examined in a coin cell configuration using 1M LiTFSI in a mixed solvent of 1,3-dioxolane and tetraethyleneglycol dimethyl ether (1:1) as the electrolyte. Li foil was used as the counter electrode. The batteries were cycled between 1.5 and 3 V using a discharge/charge rate of C/5 (334 mA g^{-1}_{sulfur}) which corresponds to a current density of 0.4 mA cm^{-2}. The discharge/charge profile is typical of a Li-S cell (**Figure 3.8a**). Two voltage plateaus are observed at ~2.4 V for the reduction of S_8 to Li_2S_4 and at ~2.0 V for the further reduction to Li_2S_2 and Li_2S. Significantly, almost no overcharge (larger charge capacity than discharge capacity) is observed on the second cycle which indicates that the sulfur shuttle mechanism has been eliminated. The favourable hydrophilic-hydrophilic interactions

between the lithium polysulfides and slightly oxidized graphene play a crucial role in reducing the loss of active mass. The long term cycling and Coulombic efficiency of the GSC is shown in **Figure 3.8b**. An initial discharge capacity of 705 mA h g^{-1}_{sulfur} at a C/5 rate (full discharge in five hours) is obtained, and the capacity only fades 8% over the first 15 cycles. The cycling stabilizes after 30 cycles and a very small capacity fade of 11% is observed between 30-50 cycles. The overall capacity fade over 50 cycles is most likely due to the formation of insulating domains of Li_2S that are not fully oxidized upon charge of the cell. The decrease in capacity can be slightly attributed to active mass loss from polysulfide dissolution, but the sulfur shuttle mechanism is minimal as evidenced by the overcharge (difference in charge capacity and discharge capacity) which is quite low and only reaches 38 mA h g^{-1}_{sulfur} at the 50th cycle. This leads to a relatively high Coulombic efficiency (for a Li-S cell) at the 50th cycle of ~93%. Although previous reports on graphene-sulfur composites have not reported this value, and hence comparison is not possible, other sulfur/carbon positive electrodes have been reported with Coulombic efficiencies as high as 94% after 50 cycles.[11] These materials were prepared by a complex, albeit clever vapour diffusion method which could make scale-up challenging. Most importantly, the overall positive electrode capacity (sulfur + carbon + binder) is 550 mA h g^{-1}_{sulfur}: over a 50% increase compared to graphene-sulfur materials recently reported.[1]

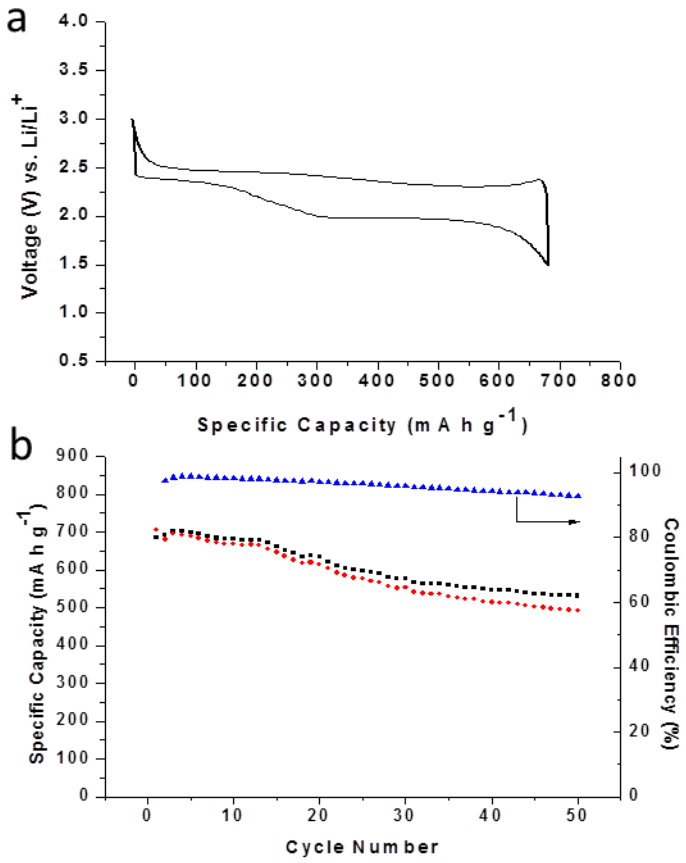

Figure 3.8 Electrochemical performance of graphene-sulfur composite (a) Galvanostatic discharge-charge of the second cycle of GSC at a current rate of C/5; (b) Cycling stability of GSC with discharge (red), charge (black) and Coulombic efficiency (blue).

3.4 Conclusions

In summary, a novel sulfur positive electrode composite has been synthesized that is easily scalable for large-scale production. The use of partially oxidized graphene as both an electrical conduit for insulating sulfur and as a barrier to retard polysulfide dissolution has led to an effective positive electrode material. The GSC is very important for realistic commercial Li-S batteries due to its extremely high sulfur content of 87 wt% and its

respectable initial discharge capacity of 705 mA h g^{-1}_{sulfur}. Further improvements are envisioned by using novel electrolytes such as ionic liquids[12], and solid polymers[13]. I have shown that large amounts of conductive carbon additives are not required to obtain an efficient working Li-S cell. This can be attributed to the promising properties of the fabrication process and the graphene composition which lies midway between highly graphitic (i.e. highly conductive) and slightly hydrophilic as a result of oxo-groups on the carbon surface, which aid in polysulfide binding. Future research is being devoted to increase the overall capacity by modifying the morphology so that more complete electrochemical reduction of sulfur can be obtained.

Chapter 4

Understanding the Nature of Absorption/Adsorption in Nanoporous Polysulfide Sorbents for the Li-S Battery

4.1 Introduction

Despite its promising attributes, the Li-S cell is plagued with problems that have hindered its widespread practical utilization. One of the main obstacles when using sulfur as a positive electrode is that it is a very good insulator. The addition of carbon to the positive electrode is highly effective at overcoming this shortcoming due to its high conductivity and low molecular weight. The other significant concern of the Li-S battery system is the rapid capacity fading and low Coulombic efficiency that is caused by the unfavourable lithium polysulfide shuttle mechanism between the negative electrode and positive electrode.[1] The lithium polysulfides derived from reduction of S_8 are soluble in organic electrolytes and can diffuse into the electrolyte and be fully reduced on the Li-metal negative electrode. These dissolved lithium polysulfides can also accumulate on the exterior surface of the carbon positive electrode and be reduced to insoluble lower order reduced sulfur species (Li_2S_2 or Li_2S). They are highly insulating, apparently blocking for ion transport, and are difficult to re-oxidize upon charge of the cell. Although many attempts have been made to overcome lithium polysulfide dissolution into the electrolyte, such as: new electrolyte systems with high viscosities,[2] Li negative electrode protection by additives (TEOS or $LiNO_3$),[3,4] or metal oxide adsorbents ($Mg_{0.6}Ni_{0.4}O$ or Al_2O_3)[5,6], these have not proven highly effective at improving the long-term cycleability of the Li-S cell while maintaining a high discharge capacity.

Recently, Ji *et al.* reported improved capacity stability by the combination of mesoporous carbon (SCM), mesoporous silica (SBA-15) and elemental sulfur as a positive electrode composite.[7] The mesoporous silica was effective at retaining the soluble lithium polysulfides at the positive electrode and limiting the fraction that take part in the sulfur shuttle mechanism. The hydrophilic pores of SBA-15 reversibly adsorbs/absorbs the hydrophilic lithium polysulfides and release them near the end of discharge so that they can be further reduced in the pores of the mesoporous carbon. This research demonstrated that cycleability in a Li-S cell can be improved with the use of a small amount of mesoporous silica in the sulfur/carbon positive electrode.

Herein, I report the use of mesoporous titania as an additive to the positive electrode in order to enhance the electrochemical performance of the Li-S system. This extends the Nazar groups previous work with mesoporous silica in hopes of finding a more commercially viable additive that is both lower cost and easier to mass produce than SBA-15.[7] Mesoporous titania is expected to function in a similar manner to mesoporous silica with the majority of lithium polysulfides being absorbed by the porous structure as illustrated in **Figure 4.1**. Moreover, titania is more electropositive than silica which could lead to significant adsorption as well. There will be an increase in the electrostatic attraction between the negative polysulfides and the oxide surface. To clarify the nature of the adsorption and/or absorption mechanism and quantify the improvement in the electrochemical performance, I used three different morphologies of TiO_2 with different physical properties (surface area, pore volume and pore size). These different mesoporous titania were used as additives to a positive electrode comprised of sulfur imbibed in a

large-pore mesoporous carbon (SCM, > 10 nm) where lithium polysulfide dissolution is more pronounced.

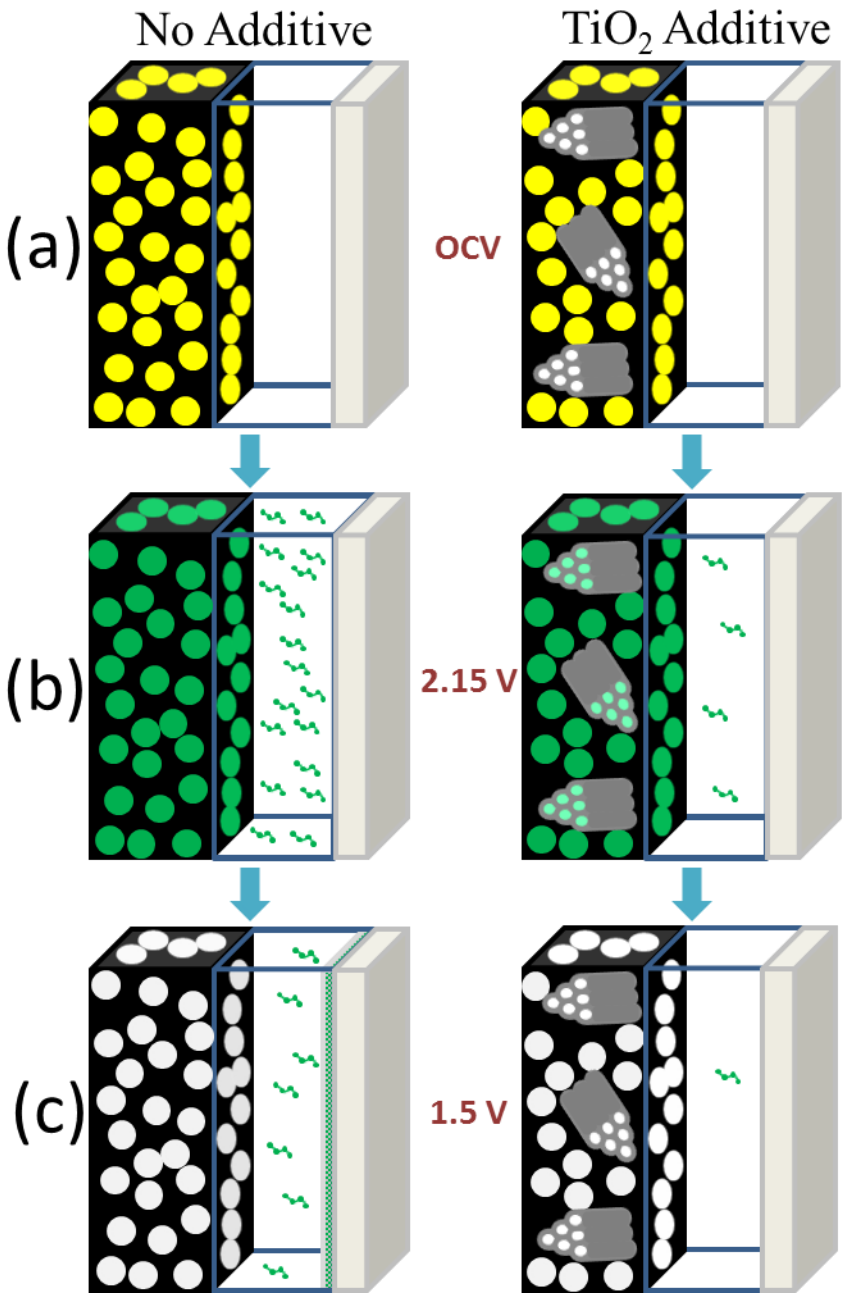

Figure 4.1 Schematic diagram illustrating the concept of polysulfide reservoirs vs. no reservoirs. Each separate image is a schematic of a Li-S cell at different stages of discharge. a) Open circuit voltage (OCV) – The cell with and without additive are

similar with no polysulfide species in the electrolyte. B) At ~ 2.15 V a high concentration of lithium polysulfides (green, S_n^{2-}, 3 < n < 8) are formed and diffuse into the electrolyte in the cell without additive. In the cell with additive, the lithium polysulfides reversibly ad/absorb in the porous TiO_2 with fewer diffusing into the electrolyte compared to the no additive cell. c) At full discharge, 1.5 V, a high concentration of lithium polysulfides diffuse back into SCM from the electrolyte and are further reduced to Li_2S, but some are reduced at the lithium metal and form a solid electrolyte interphase (green/grey film in schematic). In the cell with additive, the lithium polysulfides diffuse from the porous TiO_2 to the SCM and are fully reduced to Li_2S (grey) with fewer remaining in the electrolyte compared to the no additive cell. Black cube – carbon, clear cube – electrolyte and lithium salt, grey cube – lithium metal, yellow circle – sulfur, green circle – reduced sulfur (soluble lithium polysulfides), grey circle – fully reduced sulfur (Li_2S), green molecules in electrolyte – soluble lithium polysulfides.

4.2 Experimental

4.2.1 Preparation of positive electrode composites

The SCM carbon used as the electrical support for sulfur in this study was synthesized according to a previously described method.[7] α-TiO_2 was obtained from Mesotech Modern Materials Inc. For the synthesis of β-TiO_2 with controlled morphology, 1 g of Pluronic P123 ($EO_{20}PPO_{70}EO_{20}$) was dissolved in 10 g of ethanol at 40 ^oC. Titanium tetrachloride (1.1 ml) was added to the above solution with vigorous stirring. The mixture was stirred for 30 min and the resulting sol-gel solution was dried in an open Petri dish at 40 ^oC in air for 7 days. The as-made bulk samples were collected and calcined at

400 ^{o}C for 5 h in air. The synthesis of γ-TiO_2 is outlined in reference [9]. SBA-15 was synthesized according to a previously described method.[8] Each SCM-additive material was synthesized by mixing SCM (50 mg) and the additive (5 mg) in deionized H_2O (5 mL) and sonicating for 1 hr. The material was then stirred for a further 4 hrs and the water was evaporated in a 130 °C oven for 48 h. Sulfur was then impregnated into each SCM-additive. SCM-additive (40 mg) and sulfur (60 mg) were ground together and heated to 155 °C. For the comparison study of SCM/S-no additive, the appropriate reduction of sulfur content in the SCM was made.

4.2.2 Electrochemical analysis

Positive electrodes were constructed from 80% SCM/S-additive or SCM/S-plain, 10% poly(vinylidene difluoride) (PVdF) binder and 10% Super S carbon. The positive electrode material, ready for electrochemical studies, contained 48 wt% of sulfur as active mass and 4 wt% additive. The positive electrode material was well dispersed in cyclopentanone by sonication and slurry-cast onto a carbon-coated aluminum current collector (Exopack Advanced Coatings). Coin cells (2325 type) were constructed using an electrolyte composed of 1.0 M LiTFSI (lithium bis(trifluoromethanesulfonyl) imide) in a mixed solvent of DOL (1,3-dioxolane) and DME (1,2-dimethoxyethane) (1:1 volume ratio). Lithium metal foil was used as the negative electrode. The batteries were cycled between 1.5 and 3 V using an Arbin battery cycler at room temperature. The discharge/charge rate 1C (1672 mA g^{-1}_{sulfur}) corresponds to a current density of 1.25 mA cm^{-2}.

4.3 Results and discussion

4.3.1 Surface area, pore size/volume measurements

The nitrogen isotherms for SBA-15, α-TiO_2 and β-TiO_2 are shown in **Figure 4.2**. Previous work by the Nazar group using SBA-15 as a lithium polysulfide sorbent highlighted the effectiveness of mesoporous silica to attract and hold soluble lithium polysulfides and release them to undergo further reduction in the electrically conducting carbon matrix - SCM. The BET analysis of SBA-15 (**Figure 4.2**) shows that it has a very high specific surface area (918 $m^2 g^{-1}$) and specific pore volume (1.00 $cm^3 g^{-1}$) with a very narrow pore size distribution centered at 5.6 nm. The hysteresis in the BET isotherm is indicative of a strong capillary force in the mesopores of SBA-15 for N_2 adsorption. In the titania samples, α-TiO_2 exhibited a similar isotherm to SBA-15 with a pore size distribution centred at 5.2 nm (**Figure 4.2**). The difference is that α-TiO_2 has a significantly lower specific surface area (275 $m^2 g^{-1}$) and specific pore volume (0.41 $cm^3 g^{-1}$) compared to SBA-15 as evidenced by the decreased nitrogen uptake. β-TiO_2 was synthesized to target larger pores (9.6 nm) than α-TiO_2 in order to identify if polysulfide absorption was a function of pore size. To isolate this possible effect, the specific surface area and pore volume were kept similar between α and β-TiO_2 (**Table 4.1**). The third titania material, nanocrystalline γ-TiO_2 (details in ref [9]), was examined to determine if the surface properties of the oxide were more important than pore absorption. The γ-TiO_2 is a non-porous titania with a similar surface area to both α and β-TiO_2 (**Table 4.1**). The pore volume shown in **Table 4.1** is due to interparticle mesopores due to aggregation of the 4 - 6 nm nanocrystalline particles. Therefore, it can be determined if the lithium polysulfides interact with titania through purely adsorption, absorption or a combination of the two.

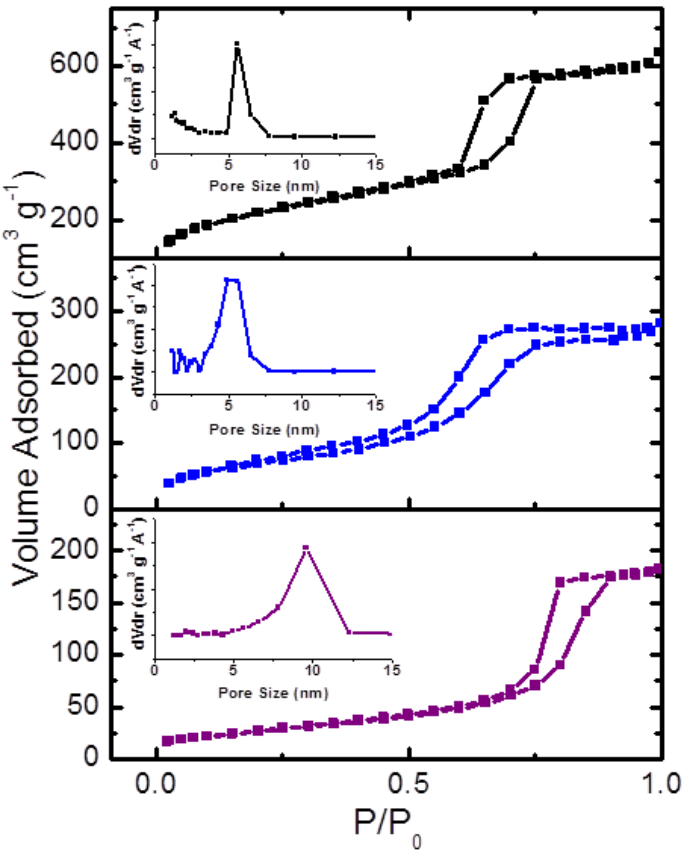

Figure 4.2 Nitrogen isotherms of SBA-15 (top, black), α-TiO_2 (middle, blue) and β-TiO_2 (bottom, purple). Pore size distributions for each additive are shown as insets in each plot. BET data for γ-TiO_2 is not shown but can be found in ref [9].

	SBA-15	α-TiO_2	β-TiO_2	γ-TiO_2
Specific Surface Area (m^2 g^{-1})	918	275	134	176
Specific Pore Volume (cm^3 g^{-1})	1.00	0.41	0.29	0.30

Table 4.1 Specific surface area and pore volume of the additives. γ-TiO_2 data taken from ref [9].

4.3.2 Electrochemical analysis

The electrochemical results of the four additives in Li-S cells are compared in **Figure 4.3**. A mesoporous carbon (pore size ~ 12 nm) termed SCM was infused with 60 wt% sulfur, and the various sorption additives were added to form a positive electrode composite. The positive electrodes were examined in a coin cell configuration using 1M LiTFSI in a mixed solvent of 1,3-dioxolane and 1,2-dimethoxyethane (1:1 vol%) as the electrolyte and were cycled at a high current rate of 1C (1675 mA g^{-1}_{sulfur}, full discharge in 1 hour). Voltage profiles of the tenth discharge of each cell are shown in **Figure 4.3a**. This data more clearly highlights the discharge characteristics since the cell has undergone a few conditioning cycles. The voltage profile for each material is indicative of a typical Li-S cell with two voltage plateaus (~ 2.3 V and ~ 2.0 V) corresponding to reduction of sulfur to high order lithium polysulfides and then to lower order lithium polysulfides. The long term cycling of the cells is shown in **Figure 4.3b** with 100 cycles shown for the SCM/S positive electrode (no additive) and 200 cycles for the SCM/S-additive positive electrodes. It is readily apparent that the addition of either SBA-15, α, or β-TiO_2 can dramatically increase the performance of the SCM/S positive electrode. The first discharge capacities and specific capacity retention of each material are given in **Table 4.2.** SBA-15 and α-TiO_2 exhibit almost identical cycling stability and high initial discharge capacities above 1200 mA h g^{-1}_{sulfur} (> 71% sulfur utilization). Even though the surface area and pore volume of α-TiO_2 is significantly less than SBA-15, the overall dimunition of lithium polysulfide dissolution is the same, as evident from the cycling stability which is almost identical. The overall effect of β-TiO_2 on cycling stability is slightly less than α-TiO_2 and SBA-15. The larger pore size of β-TiO_2 (9.6 vs ~ 5.2 nm) leads to poorer absorption

properties compared to that of the smaller pores and hence reduced effectiveness at retaining lithium polysulfides. The most surprising result is that of the positive electrode with the γ-TiO_2 additive, which showed very poor cycling stability even compared to SCM/S. This suggests that surface adsorption of polysulfide ions is not singularly effective at increasing cycling stability because the surface area is very similar between the porous and non-porous titanias (**Table 4.1**). The electrochemical results clearly show that lithium polysulfides predominantly interact with titania through an absorption mechanism.

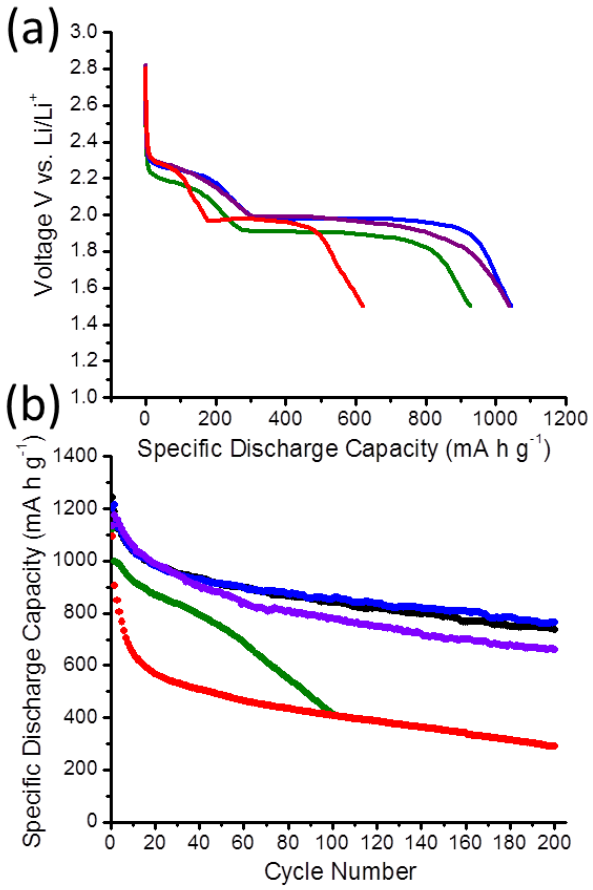

Figure 4.3 (a) Galvanostatic voltage profile of the 10th discharge and (b) Long term cycling performance of SCM/S-no additive (green), SCM/S-SBA-15 (black), SCM/S-α-TiO_2 (blue), SCM/S-β-TiO_2 (purple) and SCM/S-γ-TiO_2 (red).

	SCM/S	SCM/S-SBA-15	SCM/S-α-TiO_2	SCM/S-β-TiO_2	SCM/S-γ-TiO_2
1st cycle (mA h g^{-1})	1123	1244	1201	1135	1094
C_{100}/C_{10} (%)	45	81	82	74	63
C_{200}/C_{10} (%)	-	71	73	62	44

Table 4.2 First discharge capacity of each positive electrode material and the percentage of discharge capacity retained in each positive electrode after 100 and 200 cycles in comparison to the tenth cycle capacity.

4.3.3 Alternating current impedance spectroscopy

The stability from the porous titania additives is apparent and readily explained, but the significant decrease in discharge capacity of the SCM/S-γ-TiO_2 positive electrode material was difficult to rationalise. In order to have a comparable surface area between the non-porous and porous titania, the particle size was very small. In this case, γ-TiO_2 exhibits a particle size between 4 – 6 nm and a specific surface area of 176 m^2 g^{-1}. The porous titanias are significantly larger on the order of a few microns. Impedance studies were performed on full cells using each positive electrode material with the different additives and the Nyquist plots are shown in **Figure 4.4**. The very high frequency impedance is similar for each material, which is expected since this impedance is a measure of bulk electrolyte resistance in the cell. The high frequency (HF) semi-circle is the most noticeable difference between each material. It has been mentioned in previous studies that it is due to poor contact between particles in the electrode as opposed to a passivation layer.[10] Since these impedance data were gathered at open circuit voltage (~2.8 – 3.0 V), the electrolyte is stable and should not form a solid electrolyte interphase. The reference material is the SCM/S positive electrode as it is comprised only of sulfur and

carbon. Both the SCM/S-α-TiO_2 and SCM/S-β-TiO_2 exhibit a significantly smaller HF semi-circle than SCM/S alone. This seems to be counter-intuitive since titania is an insulator (α, β and γ-TiO_2 all have conductivities ~ 10^{-4} – 10^{-5} S cm^{-1}) and should decrease the electrical contact between SCM/S particles. However, micron sized titania as an additive has been shown in a previous report to decrease charge transfer resistance in MnO_2 electrodes and interacts favourably at the junction of MnO_2/electrolyte/carbon to increase charge transfer.[11] Although the addition of γ-TiO_2 to the positive electrode also slightly increases the degree of charge transfer, the effect is much smaller compared to the other two titania additives. This is explained by the greater number of γ-TiO_2 particles in the SCM/S matrix due to their nanoscale particle size, which appears to counteract their positive effect. The lowering of the charge transfer resistance is also observed in the voltage profiles (**Figure 4.3a**) by a decrease in over potential. Cathodes containing either α or β-TiO_2 additives, in particular, exhibit a higher discharge potential by 75 mV at a capacity of 600 mA h g^{-1}_{sulfur} *vs.* that of the SCM/S positive electrode alone.

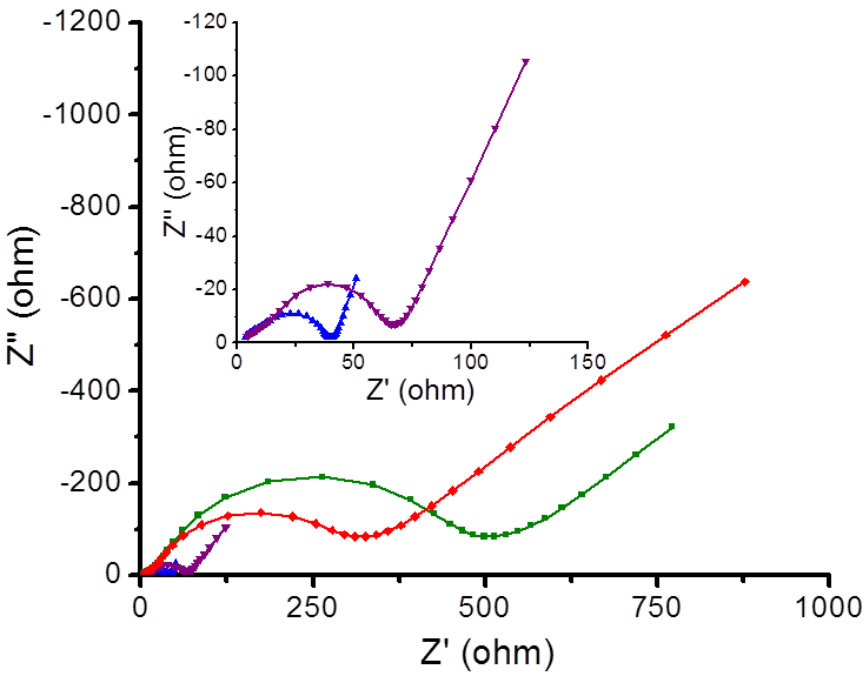

Figure 4.4 Nyquist plot of full cells containing SCM/S-no additive (green), SCM/S-α-TiO_2 (blue), SCM/S-β-TiO_2 (purple) and SCM/S-γ-TiO_2 (red). Inset: Zoom-in of the high frequency region to more clearly show SCM/S-α-TiO_2 (blue) and SCM/S-β-TiO_2 (purple).

4.3.4 Scanning electron microscopy analysis

In order to verify that mesoporous TiO_2 prevents lithium polysulfide dissolution during the electrochemical process, the electrode material from a cell containing no titania additive was compared to a cell containing α-TiO_2. SEM images of the two positive electrode materials are shown in **Figure 4.5**. Each cell was cycled for 50 cycles and the material was collected at the end of discharge at 1.5 V. The pristine, non-cycled SCM/S-plain and SCM/S-α-TiO_2 are very similar (**Figure 4.5a** and **4.5c**). However, upon cycling the SCM/S positive electrode, it is readily apparent that low order glassy lithium

polysulfides (Li_2S_2 and Li_2S) are formed on the exterior of the carbon particles. We believe these are responsible for the rapidly fading discharge capacity over 100 cycles seen in **Figure 4.3**. When the α-TiO_2 is added to SCM/S a drastic change in the surface morphology is observed. SEM micrographs reveal no glassy Li_2S phase on the surface of the material after 50 cycles. This is indicative of the ability of a polysulfide absorbent such as mesoporous TiO_2 to effectively trap polysulfides at the positive electrode and also not allow them to build up in high concentrations outside of the carbon positive electrode where they can reduce and form a highly undesirable insulating coating.

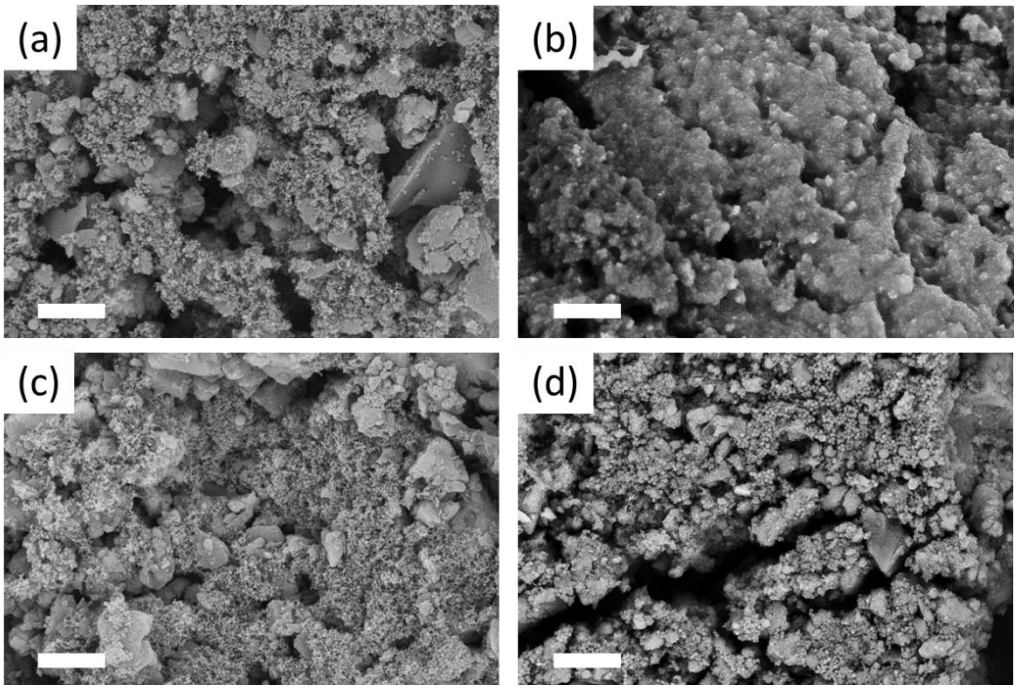

Figure 4.5 Scanning electron microscope (SEM) images of (a) SCM/S before cycling; (b) SCM/S after 50 cycles; (c) SCM/S-α-TiO_2 before cycling and (d) SCM/S-α-TiO_2 after 50 cycles. Scale bar = 5µm.

4.3.5 Fourier transform infrared and Raman spectroscopy measurements

To clarify whether titania interacts with lithium polysulfides through absorption due to the porous architecture or *via* physical/chemical adsorption, we probed the bonding interaction between titania and sulfur using FTIR and Raman spectroscopy (**Figure 4.6**). Lithium polysulfides were synthesized following a previously reported method where sulfur is reduced by lithium triethylborohydride ($LiEt_3BH$) in tetrahydrofuran.[12] Sulfur and $LiEt_3BH$ were reacted in a molar ratio of 2:1, in order to form intermediate length lithium polysulfides that are targeted at a stoichiometry of Li_2S_4. This synthesis was performed with and without α-TiO_2 present in order to probe the interaction between reduced sulfur species and titania. In **Figure 4.6a** FTIR spectra of neat Li_2S_4 and neat α-TiO_2 are compared to α-TiO_2 in the presence of Li_2S_4. The Li_2S_4 showed a characteristic S-S band (492 cm^{-1}) and α-TiO_2 displayed a Ti-O band (571 cm^{-1}). In the third spectrum - where Li_2S_4 was synthesized in the presence of α-TiO_2 - a new band appeared at 534 cm^{-1}. While this feature has not been previously reported, I hypothesise that this is due to an interaction between sulfur and titania (S-Ti-O) that can be considered as adsorption of Li_2S_4 on the surface of α-TiO_2. The Raman spectra of α-TiO_2 and α-TiO_2/Li_2S_4 also highlight the sulfur - titania interaction. Two peaks at ~395 cm^{-1} and ~525 cm^{-1} in the neat α-TiO_2 shift to ~410 cm^{-1} and ~515 cm^{-1} when Li_2S_4 is added to the system. This peak shift shows that the environment around the surface titanium atoms is altered in the presence of Li_2S_4.

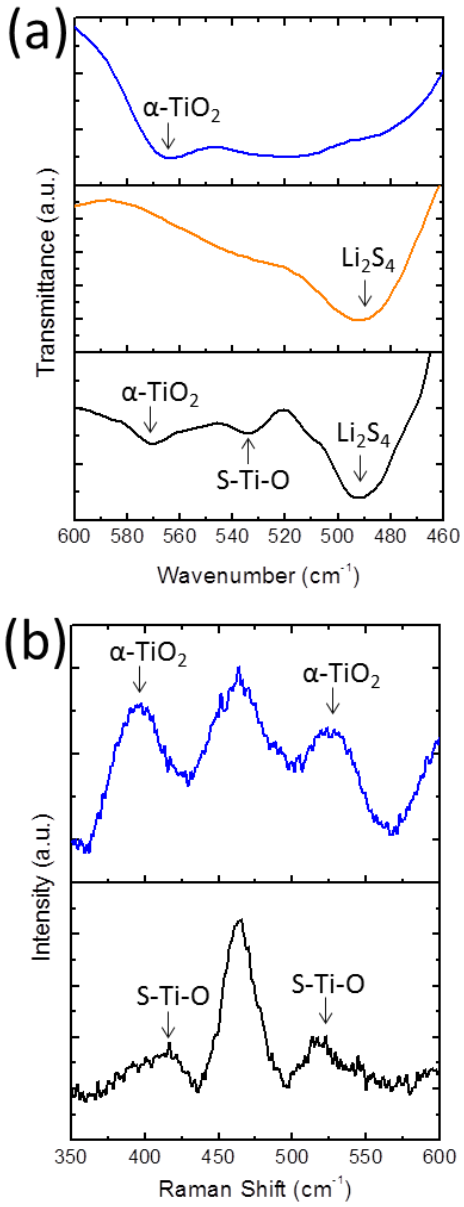

Figure 4.6 (a) FTIR spectra of neat α-TiO_2 (top, blue); neat Li_2S_4 (middle, orange) and neat α-TiO_2/Li_2S_4 (bottom, black); (b) Raman spectra of neat α-TiO_2 (top, blue) and neat α-TiO_2/Li_2S_4 (bottom, black). Peaks characteristic of the material are highlighted with arrows.

To clarify whether β-TiO_2 and γ-TiO_2 interacts with lithium polysulfides *via* physical/chemical adsorption as seen with α-TiO_2 in **Figure 4.6**, identical FTIR and

Raman analysis was carried out with β-TiO_2 and γ-TiO_2 (**Figure 4.7**). The FTIR spectrum of β-TiO_2/Li_2S_4 (**Figure 4.7a**, bottom) and γ-TiO_2/Li_2S_4 (**Figure 4.7b**, bottom) do not show any discernible new peaks corresponding to interactions between sulfur and titania (i.e. S-Ti-O) as seen in **Figure 4.6a** for α-TiO_2. In this case the Raman spectra for β-TiO_2 is more definitive (**Figure 4.7c**). There are two peaks at ~395 cm^{-1} and 510 cm^{-1} for neat β-TiO_2 and when Li_2S_4 is synthesized in the presence of β-TiO_2 these peaks do not shift (as indicated by the dotted red reference line). In the case of γ-TiO_2, the Raman spectra (**Figure 4.7d**) is more difficult to interpret and there may be a peak shift which could indicate interactions between sulfur and titania, but the sulfur signal from Li_2S_4 is too broad and strong and may envelop the titania peak. In any case, even if there is some surface interaction, γ-TiO_2's poor electrochemical performance proves that surface adsorption is not singularly enough; mesopores are key to limiting polysulfide dissolution. Therefore, enhancement of the electrochemical properties of SCM/S by α-TiO_2 can be explained as a cooperative tandem between weak adsorption on the surface and absorption by the pores that together inhibit the loss of lithium polysulfides into the electrolyte, with the latter dominating.

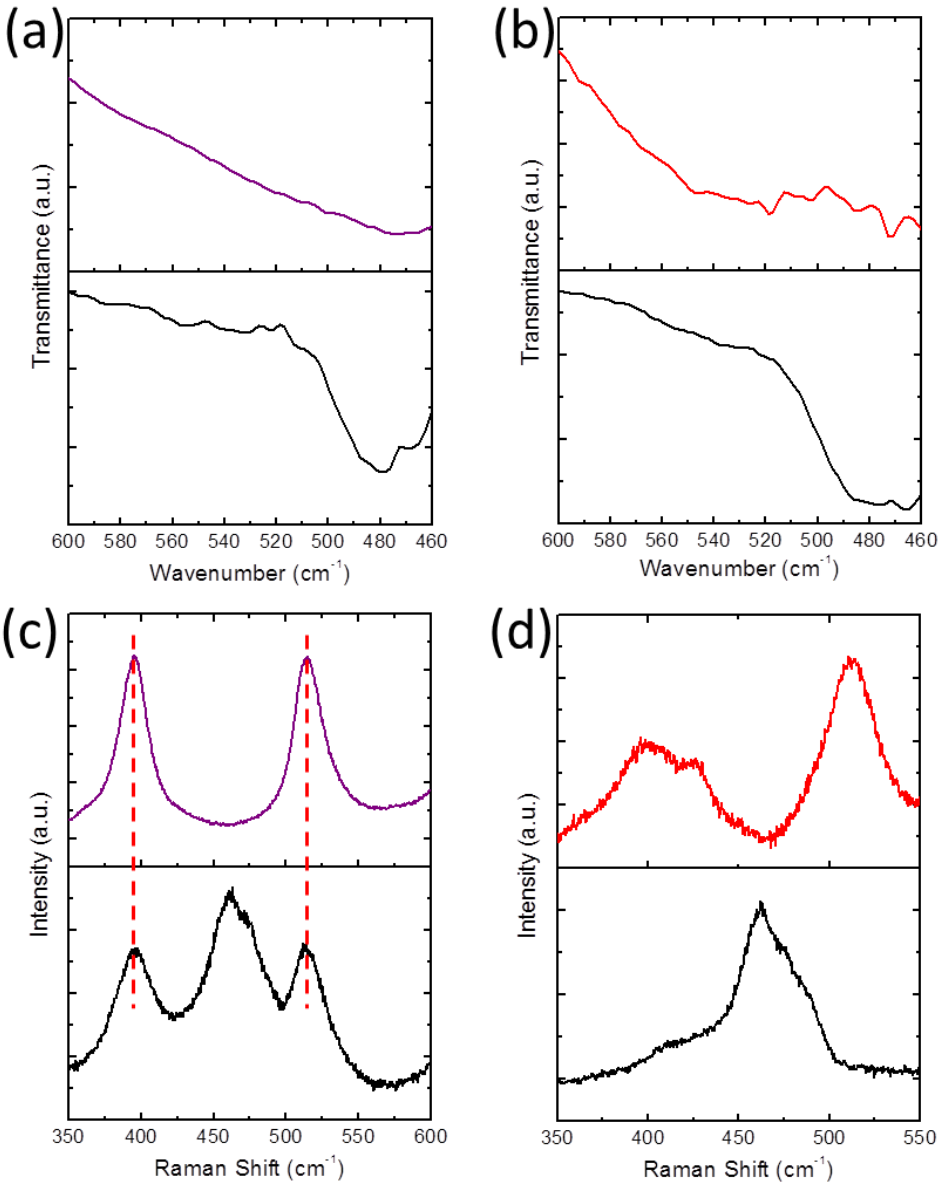

Figure 4.7 (a) FTIR spectra of neat β-TiO_2 (top, purple) and neat β-TiO_2/Li_2S_4 (bottom, black); (b) FTIR spectra of neat γ-TiO_2 (top, red) and neat γ-TiO_2/Li_2S_4 (bottom, black); (c) Raman spectra of neat β-TiO_2 (top, purple) and neat β-TiO_2/Li_2S_4 (bottom, black); (d) Raman spectra of neat γ-TiO_2 (top, red) and neat γ-TiO_2/Li_2S_4 (bottom, black).

4.4 Conclusion

In summary, I have effectively coupled mesoporous titania additives to a sulfur/carbon composite in order to improve the cycle life and capacity retention of the Li-S battery. This approach circumvents the need to apply coatings to the carbon in order to prevent or lessen polysulfide dissolution which can hinder the rate characteristics of the cell. The use of mesoporous titania particles mixed with the carbon/sulfur particles allows cycling at high C rates while maintaining discharge capacities above 750 mA h g^{-1}_{sulfur} after 200 cycles. The effect of mesoporous titania addition is significant and is achieved with only 4 wt% additive. Future work will study the interaction between various metal oxides and lithium polysulfides in order to determine the optimum combination of pore size, surface area and adsorption characteristics.

Chapter 5

Sulfur Filled Porous Carbon Spheres with Greater than 100% Capacity Retention after 100 Cycles at Super-High Rate

5.1 Introduction

Encompassing sulfur in mesoporous carbons of varying pore size has been extensively researched in the past few years with great success.[1,2,3,4,5,6] Sulfur is readily absorbed in most mesoporous carbons and when reduced to lithium polysulfides are effectively trapped in the inner channels of the pores of the carbon.[1] A clear limitation of this technique is that the diffusion length of lithium ions can vary between separate carbon particles and uniformity at the nanoscale is difficult to achieve. To resolve this issue, spherical carbon particles can be synthesized with nanoscale homogeneous diameters that will decrease the lithium ion diffusion length and therefore, increase rate capability. Herein, I report a novel method of sulfur encapsulation through the use of porous carbon spheres (PCS). Shown in **Figure 5.1** is a schematic illustration of the simple synthetic procedure used to create PCS's stuffed with sulfur.

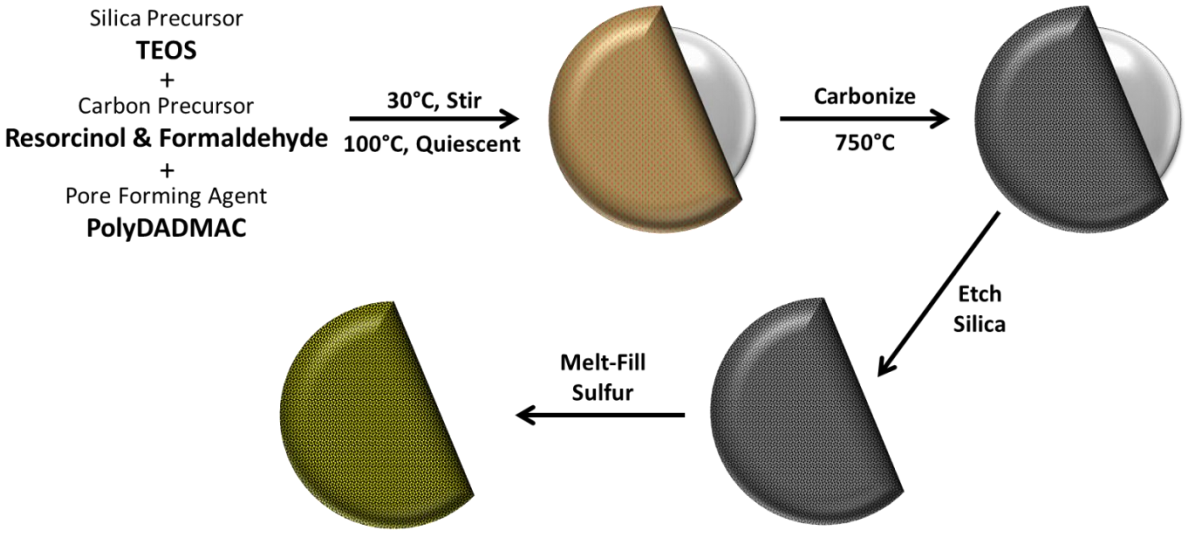

Figure 5.1 An illustration of the synthetic procedure to produce porous carbon spheres with a sulfur filled shell.

5.2 Experimental

5.2.1 Synthesis of porous carbon spheres

The synthetic procedure is an adaptation of a report by Fuertes *et al.*[7] In order to introduce porosity in the shell of the carbon spheres; a cationic polymer was introduced following an adaptation of a report by Bruno *et al.*[8] In a typical synthesis, 11.4 mL ammonium hydroxide is added to a solution of ethanol (244 g) and deionized water (40 g) in a 1 L round bottom flask with stirring at 30 °C. After stirring for 30 minutes, 11.2 mL tetraethyl orthosilicate (TEOS) is added under vigorous stirring. In a separate vial, 1.6 g resorcinol, 2.24 mL formalin and 240 μL poly(diallyldimethylammonium chloride) (7 wt% in deionized water) were mixed and added to the previous solution after 10 minutes. The solution was kept stirring at 30 °C overnight. The solution was then transferred to a hydrothermal bomb and kept at 100 °C overnight in static condition. The resultant brown precipitate was centrifuged and washed 3 times each with deionized water and ethanol and

was dried at 70 °C overnight. The dry brown polymer was carbonized under flowing argon gas (ramp 3.75 °C/min to 750 °C and hold 60 minutes). The resultant carbon coated silica was treated in 15% hydrofluoric acid to etch and remove the inner silica core.

The PCS's were impregnated with 68 wt% sulfur by a melt-diffusion method. Typically, 30 mg PCS and 70 mg sulfur were ground together in a mortar and pestle and were then pressed in a pellet die and placed in an oven at 155 °C overnight. In the process some sulfur is evolved, resulting in the slightly lower sulfur composition in the final PCS/S-68% composite.

5.2.2 Electrochemical analysis

Positive electrodes were constructed from 80% PCS/S-68%, 10% Kynar Powerflex binder and 10% Super S carbon. The positive electrode material ready for electrochemical studies contained 54 wt% of sulfur as active mass. The positive electrode material was well dispersed in dimethylformamide by sonication and slurry-cast onto a carbon-coated aluminum current collector (Exopack Advanced Coatings). Coin cells (2325 type) were constructed using an electrolyte composed of 1.0 M LiTFSI (lithium bis(trifluoromethanesulfonyl) imide) in a mixed solvent of DOL (1,3-dioxolane) and DME (1,2-dimethoxyethane) (1:1 volume ratio) with 2 wt% $LiNO_3$ as additive . Lithium metal foil was used as the negative electrode. The batteries were cycled between 1.5 and 3 V using an Arbin battery cycler at room temperature. The discharge/charge rate 1C (1672 mA g^{-1}_{sulfur}) corresponds to a current density of 1.25 mA cm^{-2}.

5.3 Results and discussion

5.3.1 Surface area, pore size/volume measurements

The PCS's exhibit favourable structural properties for use as a host for sulfur. The nitrogen isotherms and pore size distributions of bare and sulfur filled PCS's are shown in **Figure 5.2**. Before sulfur impregnation the PCS's have high specific surface area (824 m^2 g^{-1}) and specific pore volume (3.42 cm^3 g^{-1}) with a narrow pore size distribution centred at 4.3 nm. The cationic polymer poly(diallyldimethylammonium chloride) was effective at introducing porosity in the carbon shells. The pores were limited to a size regime that is known to limit polysulfide dissolution.[1,4] The specific pore volume of the mesopores is 1.62 cm^3 g^{-1} and this can accommodate 77 wt% sulfur. Slightly less sulfur (68 wt%) was impregnated in the spheres to allow for volume expansion upon reduction to Li_2S. After impregnation with sulfur, the specific surface area and specific pore volume dramatically decreased (108 m^2 g^{-1} and 0.41 cm^3 g^{-1}) and the pore size distribution shows an absence of pores. In both cases the majority of the pore volume occurs at high relative pressure and is due to large void volumes (interior of the spheres).

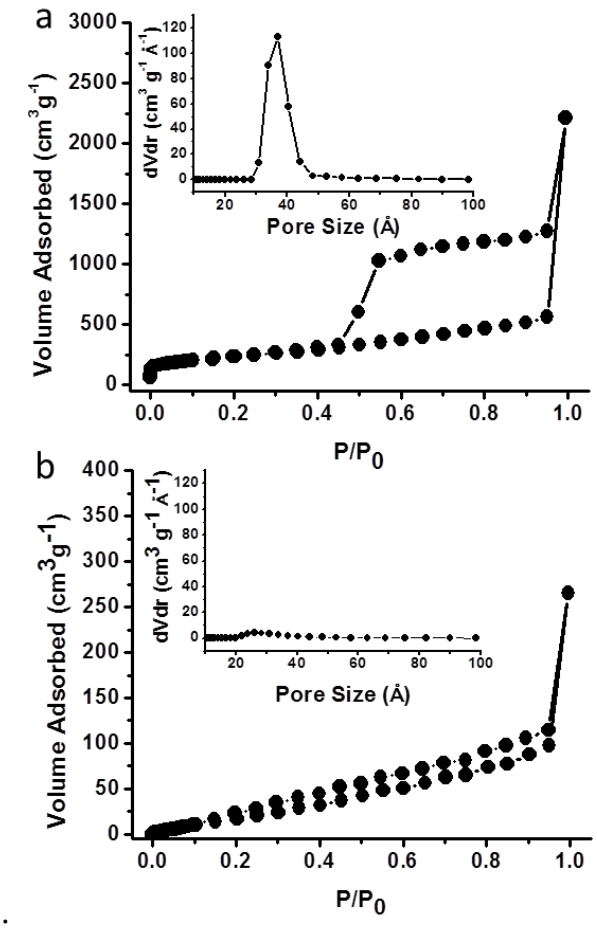

Figure 5.2 Nitrogen isotherms of (a) PCS and (b) PCS/S-68%. Pore size distributions are shown as insets in each plot.

5.3.2 Thermogravimetric analysis

The PCS's are then impregnated with sulfur by melt-diffusion at 155 °C. Sulfur liquid is drawn into the mesopores in the shell by capillary force. Thermogravimetric analysis was performed to determine the exact sulfur content imbibed in the PCS's and is shown in **Figure 5.3**. Sulfur mass is lost in two distinct temperature regions in the plot. Below 280 °C, 58 wt% sulfur is lost and is believed to be the bulk sulfur that is infiltrated in the mesopores of the carbon shell. Above 280 °C, 10 wt% sulfur evolves with weight

loss continuing to 420 °C. This high temperature sulfur must be highly confined in the porous shell structure. In this case sulfur that evolves at these extreme temperatures can play an important role in stable cycling of a Li-S cell because the sulfur is highly confined.[9] The final composite comprises 68 wt% sulfur and will be defined as PCS/S-68%.

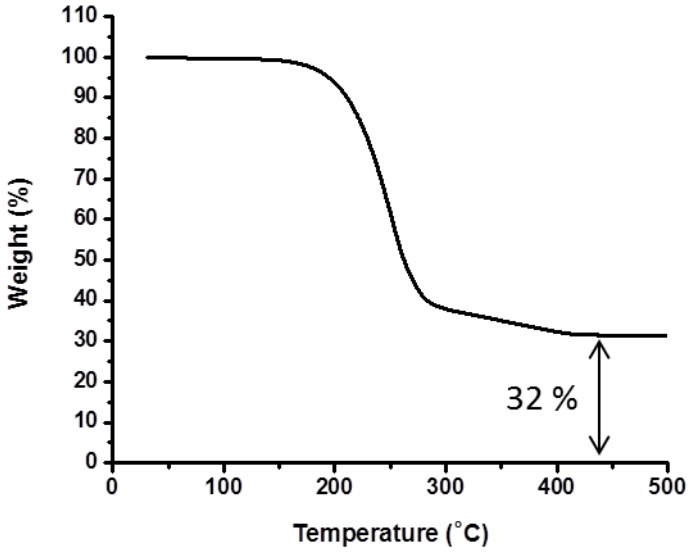

Figure 5.3 TGA curve (N_2 atmosphere) of PCS/S-68%, showing weight loss of 68% corresponding to the loss of sulfur.

5.3.3 Scanning electron microscopy and scanning transmission electron microscopy analysis

The Stober method is used to synthesize highly uniform silica spheres that are then encased by a carbon precursor polymer. The polymer coating is carbonized at 750°C and the internal silica core is removed by HF treatment. The final homogeneous PCS's are imaged by SEM and shown in **Figure 5.4**. The PCS's with and without sulfur impregnation were also imaged by STEM in **Figures 5.5** and **5.6**. In **Figure 5.5a** a single

PCS particle is shown with a diameter of ~220 nm and a shell thickness of ~20 nm. The surface of the particle shows disordered porosity and is in agreement with porosity found through nitrogen adsorption measurements. An energy dispersive X-ray spectroscopy line scan is shown in **Figure 5.5a** as an overlay of the PCS particle it was performed on as well as in separate plots for each element carbon and sulfur. Carbon is found throughout the particle and has a slightly larger signal at the edge of the sphere. Shown in **Figure 5.6a** is a STEM image of a PCS/S-68% particle. The morphology of the particle did not change upon sulfur impregnation and the diameter and shell thickness remained constant as well. In order to determine if sulfur impregnated the PCS's shell, an energy dispersive X-ray spectroscopy line scan is shown on a PCS/S-68% particle in **Figure 5.6b**. The carbon signal is similar to the PCS particle without sulfur (**Figure 5.5b**), but the sulfur signal shows a homogeneous distribution of sulfur throughout the particle. This proves that sulfur is found in the mesopores of the carbon shell and not in the interior void of the sphere. If sulfur was present in the interior void the signal would increase throughout the center of the particle.

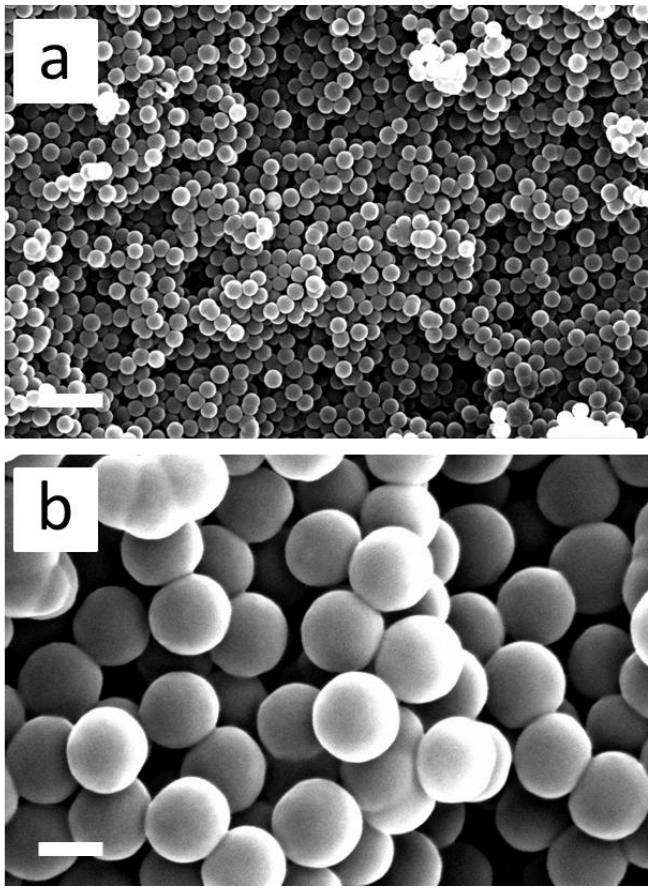

Figure 5.4 SEM images of PCS's prior to sulfur impregnation. a) low magnification, scale bar is 1 μm; b) high magnification, scale bar is 200 nm.

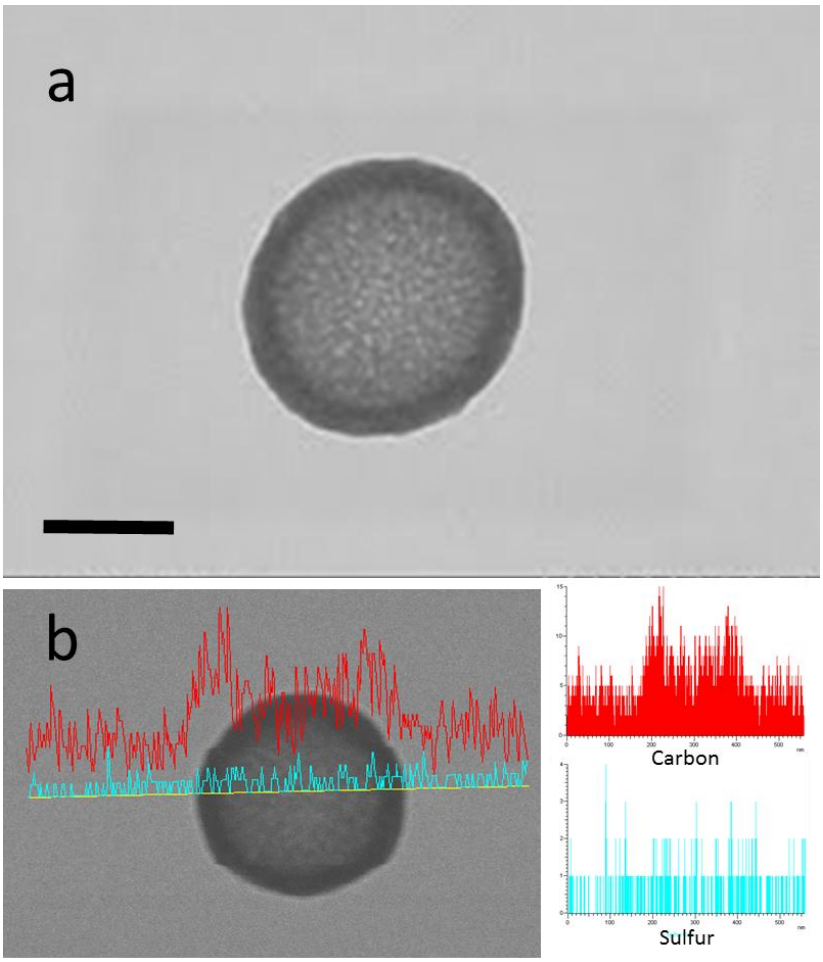

Figure 5.5 a) STEM image of PCS prior to sulfur impregnation (scale bar 100 nm); b) STEM image of PCS and energy dispersive x-ray spectroscopy line scan showing carbon and sulfur distribution.

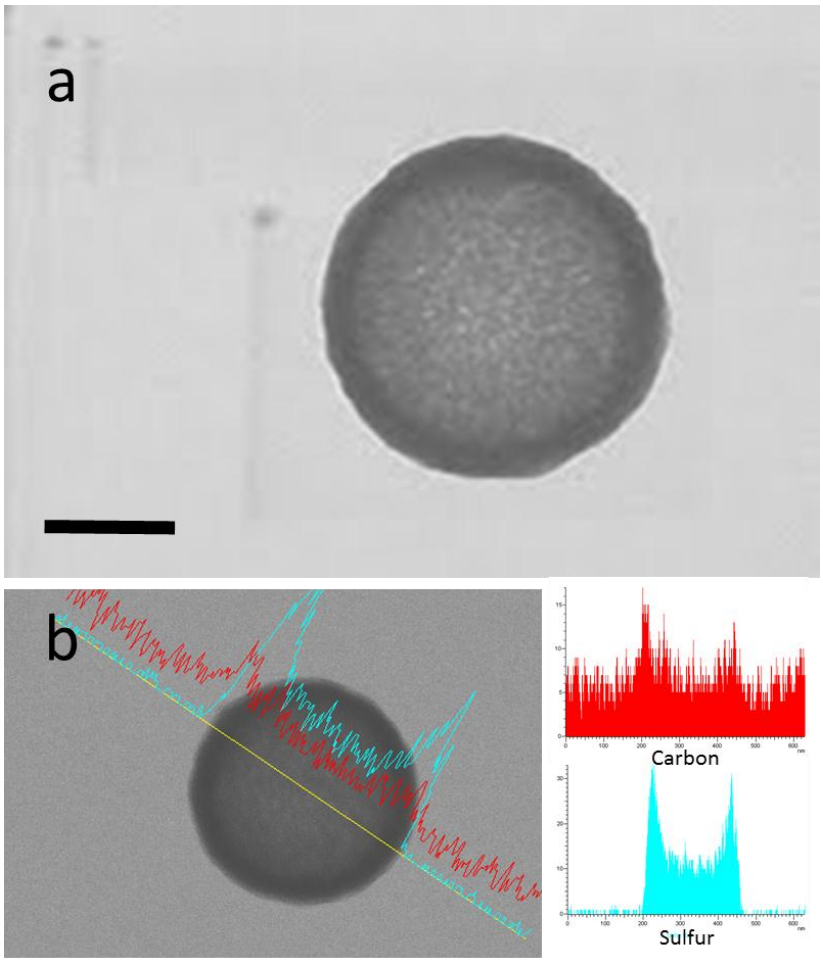

Figure 5.6 a) STEM image of PCS/S-68% (scale bar 100 nm); b) STEM image of PCS/S-68% and energy dispersive x-ray spectroscopy line scan showing carbon and sulfur distribution.

5.3.4 Electrochemical analysis

The electrochemical properties of PCS/S-68% were examined in a coin cell configuration using 1M LiTFSI in a mixed solvent of 1,2-dimethoxyethane and 1,3-dioxolane with 2 wt% $LiNO_3$ as additive for protection of the lithium foil negative electrode. The batteries were cycled between 1.5 and 3.0 V at a high discharge/charge rate of 1C (1672 mA g^{-1}_{sulfur}) for long term cycling and varying rates to determine high rate

capability. The first and 100th voltage profiles are shown in **Figure 5.7** and display the typical two voltage plateau (~2.3 V and ~2.0 V vs. Li/Li+) of Li-S cells. The first discharge capacity is low when considering the theoretical specific discharge capacity of sulfur (1672 mA h g^{-1}_{sulfur}), but the capacity increases over 100 cycles by 8%. Capacity retention is pivotal for real-world applications as consumers do not want the performance of their phones/laptops/cars etc. to be reduced over cycle life.

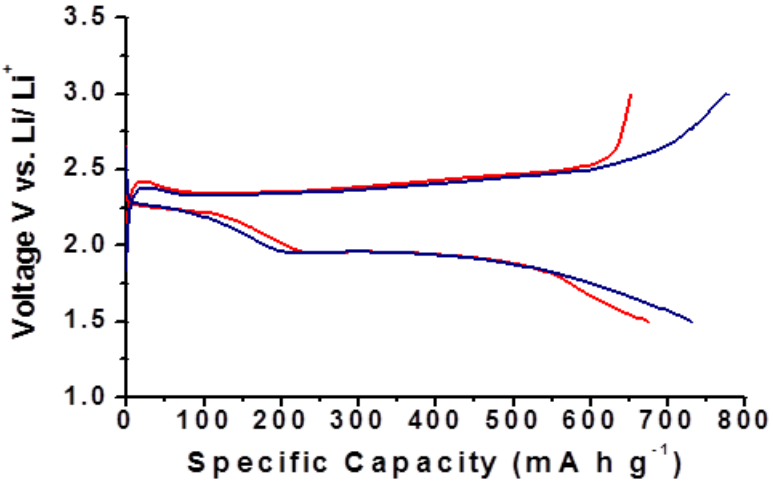

Figure 5.7 Galvanostatic voltage profiles of the 1st (red) and 100th (blue) cycles of PCS/S-68%.

The long term cycling of PCS/S-68% exhibits outstanding capacity retention at a high rate that represents full discharge of the cell in one hour (**Figure 5.8**). Previous reports have displayed high capacity retentions in excess of 90% over 100 cycles, but have fallen short at achieving this benchmark above C/2 rates (full discharge in 2 hours).[6] The specific discharge capacity experiences a slight fade over the first few cycles that have recently been reported as an activation step, whereby all of the sulfur in the composite is not fully accessible to electrolyte initially because the pores are filled.[10] The sulfur in the

porous carbon shell must first be reduced in order for electrolyte and Li ions to fully penetrate into the inner void of the spheres. After the first few activation cycles, the capacity stabilizes at an average value of 726 mA h g^{-1}_{sulfur} over 100 cycles. The capacity retention with respect to the first cycle discharge capacity remains above 100% after activation and for the duration of 100 cycles.

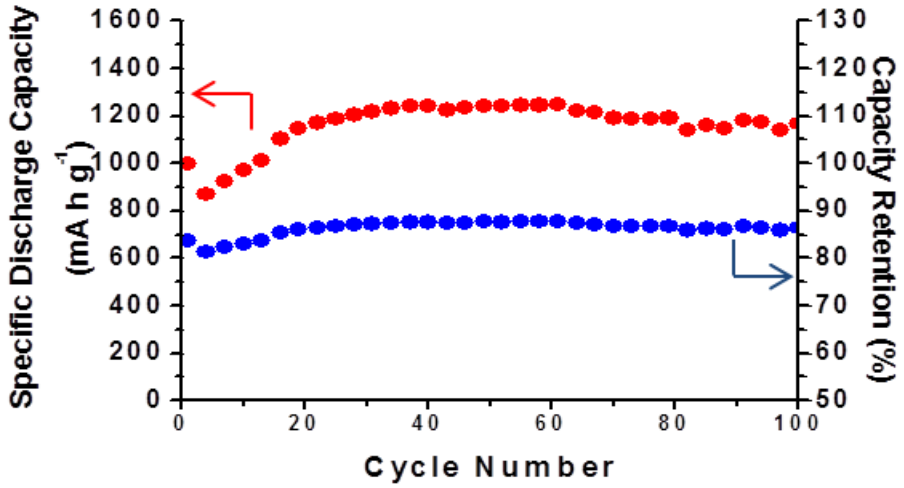

Figure 5.8 Long-term cycling of PCS/S-68% at 1C rate. The specific discharge capacity in mA h g^{-1} is represented on the left y-axis and capacity retention is represented on the right y-axis.

For practical purposes, Li-S cells must also be able to cycle at different current densities as different devices will require varying discharge rates. Rate testing was performed on PCS/S-68% using the same coin cell configuration and electrolyte as was used for the long term cycling experiment (**Figure 5.9**). The cell was cycled at C/2 rate (full discharge in 2 hours) for the initial five cycles and showed a high initial discharge capacity of 1215 mA h g^{-1}_{sulfur} and slightly faded over five cycles. The current was increased to a 1C rate and the capacity decreased slightly but was considerably more stable

at the higher rate. The rate was further increased to 2C and 3C (full discharge in 20 minutes) and the capacity only decreased to 600 mA h g^{-1}_{sulfur} after 10 cycles at the highest rate. The remarkable electrochemistry of this material was further highlighted by decreasing the current density back to a 1C rate, where ~ 87% capacity was retained from the average capacity during cycles 6 to 15 at 1C rate.

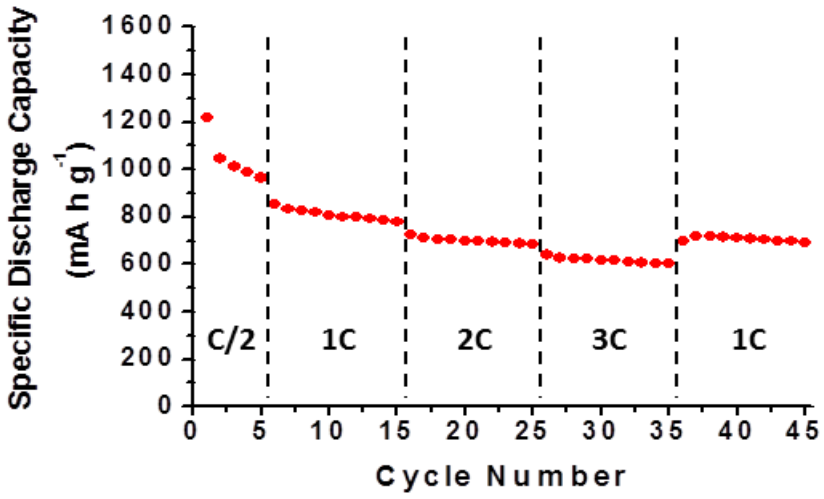

Figure 5.9 Rate capability profile of PCS/S-68% over 45 cycles at various rates.

5.4 Conclusion

In summary, I have successfully synthesized porous carbon spheres and infiltrated them with sulfur to produce a Li-S battery with very stable long-term cycling. Through the use of a spherical carbon framework, a highly uniform positive electrode material is formed and the lithium diffusion length is ideally shorter and more equivalent from particle to particle. PCS/S-68% exhibited superior electrochemical results with greater than 100% capacity retention after 100 cycles at a high 1C rate. This is particularly good news for the practical commercial use of Li-S batteries as it addresses the issue of fading capacity over the life of the battery. The rate capability of PCS/S-68% is also very good,

with the ability to be discharged up to 3C while maintaining over 600 mA h g^{-1}_{sulfur} capacity. PCS's represent a highly viable avenue for Li-S battery technology due to their ease of scale-up as well as their uniformity in size and composition.

Chapter 6

Carbide Derived Carbons as Microporous Hosts for Sulfur in a Lithium-Sulfur Battery

6.1 Introduction

Mesoporous carbons have been the main research focus for conductive hosts of sulfur in the Li-S battery. There have been few reports on the use of microporous carbons serving the same role that mesoporous carbons have performed quite effectively. Micropores are defined by IUPAC as pores less than 2 nm in diameter. In the recent literature on Li-S batteries there have been different forms of microporous carbons used; activated carbon cloth[1], sucrose derived microporous carbon[2] and nickel templated microporous carbon[3]. Of the three materials, the activated carbon cloth had the highest discharge capacity but had low sulfur content. The sucrose derived carbon exhibited stable cycling but was not practical at higher sulfur contents than 41 wt% due to a significant drop in overall capacity. Nickel templated microporous carbon exhibited very stable cycling and a high discharge capacity at low rates, but experienced significant capacity loss at higher rates. Herein, carbide derived carbons (CDC's) will be used as hosts for sulfur in a Li-S battery. CDC's are synthesized by removing the metal atom from a metal carbide through chlorine etching, leaving a micropore in place of where the metal atom resided. This method produces a highly uniform porosity in the micropore regime and is highly tunable due to the variety of metal carbides available. The parameters that can be altered are; type of metal carbide and the chlorination temperature which alters the pore size and graphitization of the resultant microporous carbon.[4] The aim of using CDC's as hosts for

sulfur is to attempt to confine sulfur inside the micropores and limit its dissolution into the electrolyte through confinement as it is reduced to lithium polysulfides.

6.2 Experimental

6.2.1 Synthesis of carbide derived carbon

Carbide derived carbon synthesis is carried out as previously reported by Svensson *et al.*[5]. TaC (99%, < 5μm) is put into a quartz boat and loaded into a quartz tube in a tube furnace. The tube furnace is equipped with both Ar and Cl_2 gas and the output is run into a 1M NaOH bath to neutralize the outgoing Cl_2 gas. The system is under Ar flow as the temperature is heated to 900 °C in 3 hours. Once the chlorination temperature is reached the flow of Ar is stopped and Cl_2 gas enters the system. The system is maintained at 900 °C for 3 hours under Cl_2 gas flow (reaction equation is shown below). Cl_2 gas flow is stopped and Ar is reintroduced into the system as the temperature is raised to 1000 °C over 30 min and held there for 1 hour. This step ensures the removal of any excess Cl_2 trapped in the CDC. The final step is cooling of the system over 3 hours under Ar flow. The resultant CDC is then immersed in deionized water and stirred for 3 hours to ensure complete removal of Cl_2 from the CDC. The CDC is then dried overnight at 150 °C.

Chlorination Reaction: $M_xC_{y(s)} + (z/2)Cl_{2(g)} \rightarrow xMCl_{2(g)} + yC_{(s)}$

where M - metal, C – carbon, Cl - chlorine

Two different CDC's were examined in this work. The first used TaC from Sigma Aldrich with no pre-treatment and the second CDC used a planetary ball mill to reduce the TaC particle size prior to chlorination. Typically, 10 g of TaC (99%, < 5μm) was loaded into a silicon nitride container with silicon nitride balls and milled for 12 hours at 300 rpm.

6.2.2 Carbide derived carbon/sulfur composite – Melt-diffusion

The CDC was impregnated with 40 wt% sulfur by a melt-diffusion method. Typically, 60 mg CDC and 40 mg sulfur were ground together in a mortar and pestle and were then pressed in a pellet die and placed in an oven at 155 °C overnight.

6.2.3 Carbide derived carbon/sulfur composite – Agitation-friction

The CDC was infiltrated with 40 wt% sulfur by an agitation-friction method[6]. Typically, 60 mg CDC and 40 mg sulfur were added to 500 mL deionized water in a 1 L round bottom flask. The suspension was stirred overnight at 1000 rpm. The material was collected by filtration and dried overnight at 60 °C.

6.2.4 Carbide derived carbon/sulfur composite – Vapour-infusion

The CDC was infiltrated with sulfur by a vapour-infusion technique. Typically, 50 mg CDC is loaded into an 8 x 10 mm quartz tube sealed at one end. Then glass wool is inserted into the tube followed by 1 g of sulfur and another piece of glass wool. The tube is then evacuated and sealed. The tube is loaded into an open steel tube and put into a tube furnace. The tube is heated to 600 °C over 2 hours and remains at this temperature for 1 hour. The material is then cooled to room temperature over 2 hours. This method puts an excess amount of sulfur into the CDC and post-treatment must be performed by heating the material in flowing Ar gas to a desired temperature to remove the excess sulfur.

6.2.5 Electrochemical analysis

Positive electrodes were constructed from 80% CDC/S, 10% Kynar Powerflex binder and 10% Super S carbon. The positive electrode material was well dispersed in dimethylformamide by sonication and slurry-cast onto a carbon-coated aluminum current

collector (Exopack Advanced Coatings). Coin cells (2325 type) were constructed using an electrolyte composed of 1.0 M LiTFSI (lithium bis(trifluoromethanesulfonyl) imide) in a mixed solvent of DOL (1,3-dioxolane) and DME (1,2-dimethoxyethane) (1:1 volume ratio) with 2 wt% $LiNO_3$ as additive . Lithium metal foil was used as the negative electrode. The batteries were cycled between 1.5-3 V or 1.9-2.6 V using an Arbin battery cycler at room temperature. The discharge/charge rate C/10 (168 mA g^{-1}_{sulfur}) and C/2 (836 mA g^{-1}_{sulfur}) corresponds to a current density of 0.25 mA cm^{-2} and 0.63 mA cm^{-2} respectively.

6.3 Results and discussion

6.3.1 Bulk carbide derived carbon

6.3.1.1 Scanning electron microscopy analysis

SEM was used to analyze bulk TaC pre and post chlorination at 900 °C and is shown in **Figure 6.1**. Before chlorination the TaC particles have an irregular morphology and vary in size, with most particles exhibiting a size greater than 1 μm (**Figure 6.1a**). After Cl_2 treatment, the CDC exhibits a similar morphology and particle size with untreated TaC (**Figure 6.1b**). This is expected because the removal of tantalum from the structure only creates a pore and the remaining carbon atoms retain the previous structure.

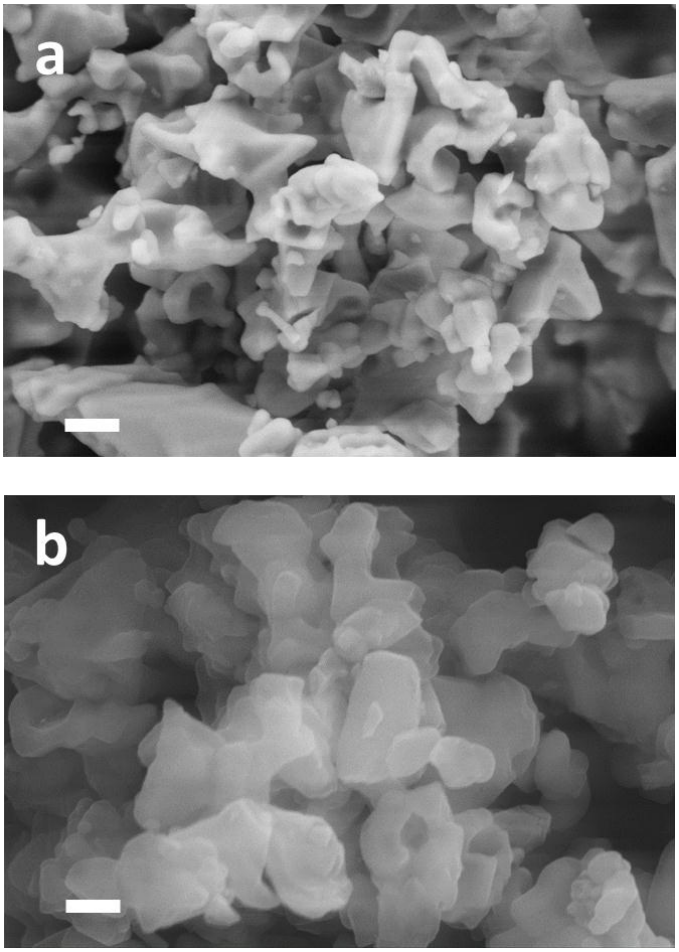

Figure 6.1 SEM images of a) TaC prior to chlorination, scale bar is 500 nm; b) TaC after chlorination, scale bar is 500 nm.

6.3.1.2 Surface area, pore size/volume measurements

The synthetic process of removing a metal atom from a metal carbide is a highly effective method to synthesize a purely microporous material. However, the porosity and pore size distribution is dependent on the temperature at which chlorination is performed. As chlorination temperature increases, the pores increase in size and at high enough temperatures (> 1000 °C) there can be formation of small mesopores.[5] The focus of this work is on microporous carbons, so the synthesis temperature remained below 1000 °C.

The nitrogen isotherm of bulk-CDC is shown in **Figure 6.2a**. The isotherm shows the typical IUPAC profile for a microporous material with a sharp nitrogen uptake at very low pressure where nitrogen quickly fills the micropores. There is minimal hysteresis at higher pressures and any mesoporosity is most likely attributed to interparticle nitrogen adsorption. The overall pore volume is 1.58 $cm^3 g^{-1}$ and the total surface area is 2003 $m^2 g^{-1}$. The pore size distribution of bulk-CDC is shown in **Figure 6.2b**. Analysis of micropores by nitrogen adsorption requires a different analysis technique than for mesopores. Quenched solid density functional theory (QSDFT) analysis is used to determine the pore size distribution and the cumulative volume of all pores. The porosity of bulk-CDC is mostly comprised of micropores with a size < 1 nm and larger micropores < 2 nm. The pore volume contributed by the micropores is ~0.8 $cm^3 g^{-1}$.

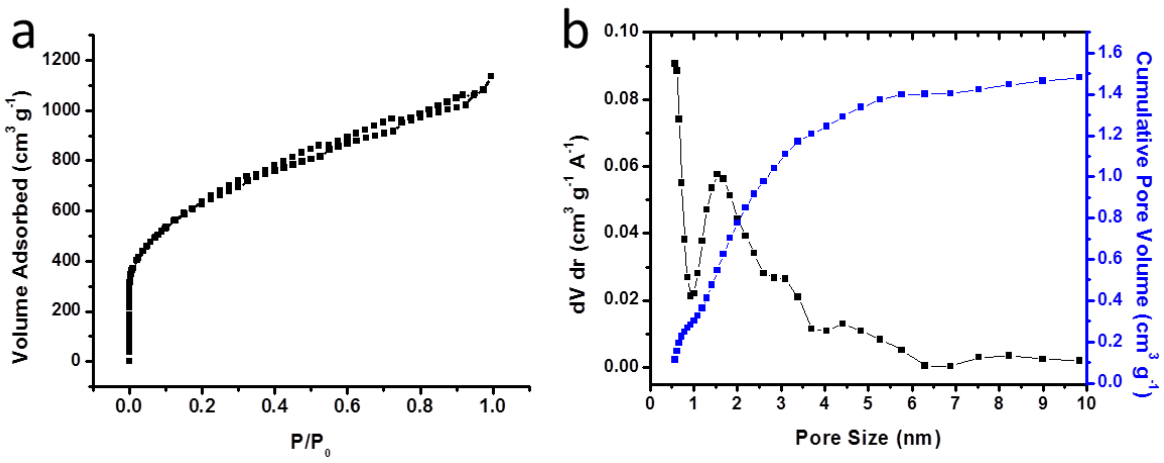

Figure 6.2 a) Nitrogen isotherm of bulk-CDC; (b) Pore size distribution of bulk-CDC.

6.3.1.3 Thermogravimetric analysis

Bulk-CDC was impregnated with sulfur using two different techniques. The pore volume of the micropores determined by QSDFT analysis should allow incorporation of

~45% sulfur. Slightly less sulfur was used as all of the micropores are not likely accessible to impregnation. The first technique used was melt-diffusion whereby sulfur and bulk-CDC are pressed into a pellet and heat treated at 155 °C (bulk-CDC-MD). The second technique was agitation-friction whereby sulfur and bulk-CDC are stirred in water at high speed and the friction between the particles forces impregnation of sulfur into the CDC's micropores (bulk-CDC-AF). Shown in **Figure 6.3** are the TGA curves for each material. Bulk-CDC-MD has 42 wt% sulfur impregnated and bulk-CDC-AF has 40 wt% sulfur infiltrated into its structure.

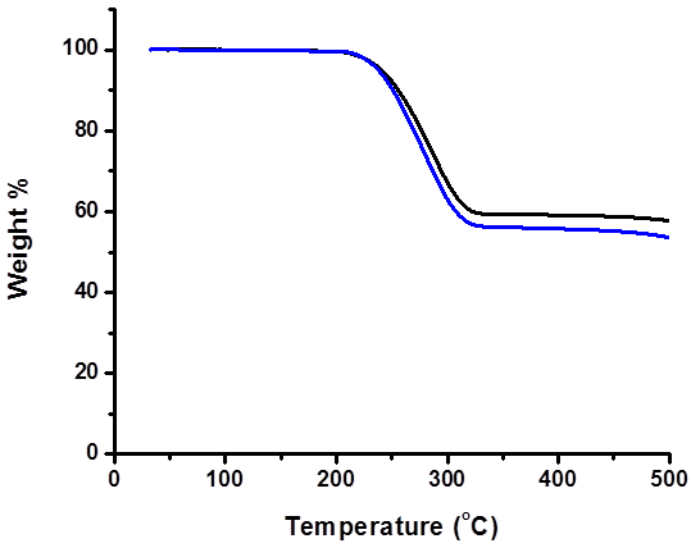

Figure 6.3 TGA curve (N_2 atmosphere) of bulk-CDC-MD (blue) and bulk-CDC-AF (black).

6.3.1.4 Electrochemical analysis

The electrochemical properties of bulk-CDC-MD and bulk-CDC-AF were examined in a coin cell configuration using 1M LiTFSI in a mixed solvent of 1,2-dimethoxyethane and 1,3-dioxolane with 2 wt% $LiNO_3$ as additive for protection of the lithium foil negative

electrode. The batteries were cycled between 1.5 and 3.0 V at a low discharge/charge rate of C/10 (168 mA g^{-1}_{sulfur}). The electrochemical properties of the two different sulfur impregnation techniques are directly compared in **Figure 6.4**. The first discharge profile (**Figure 6.4a**) of each material display the typical two voltage plateau (~2.3 V and ~2.0 V vs. Li/Li^+) of Li-S cells. Bulk-CDC-AF has a higher initial discharge capacity than bulk-CDC-MD, but both cells experience significantly less charge capacity than discharge capacity. The long term cycling of each material is shown in **Figure 6.4b**. Over 30 cycles bulk-CDC-AF has both a higher overall capacity and a slightly larger capacity retention than bulk-CDC-MD. The low overall capacity and poor capacity retention of both materials can be attributed to the large particle size of the CDC's. The interior micropores are difficult to access by simple agitation-friction and in the next section the particle size will be reduced to introduce more surface area and micropores to sulfur.

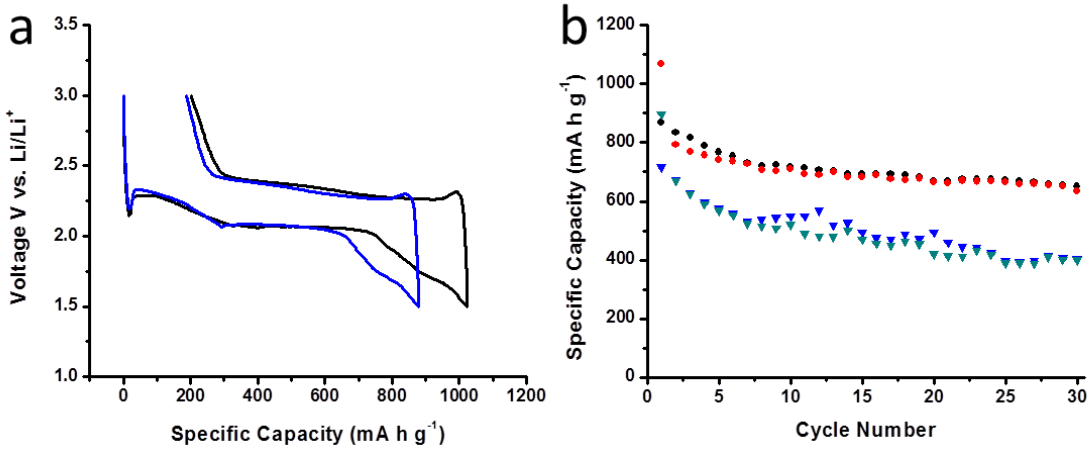

Figure 6.4 a) Galvanostatic voltage profile of the first cycle of bulk-CDC-MD (blue) and bulk-CDC-AF (black); (b) Long term cycling of bulk-CDC-MD (discharge, green; charge, blue) and bulk-CDC-AF (discharge, red; charge, black) at C/10 rate.

6.3.2 Nano carbide derived carbon

6.3.2.1 Scanning electron microscopy analysis

In order to decrease the particle size, bulk TaC was ball-milled for 12 hours at 300 rpm. The particle size decreased significantly with the majority of particles having a size < 500 nm (**Figure 6.5a**). After chlorination the particles retained the same morphology and particle size (**Figure 6.5b**).

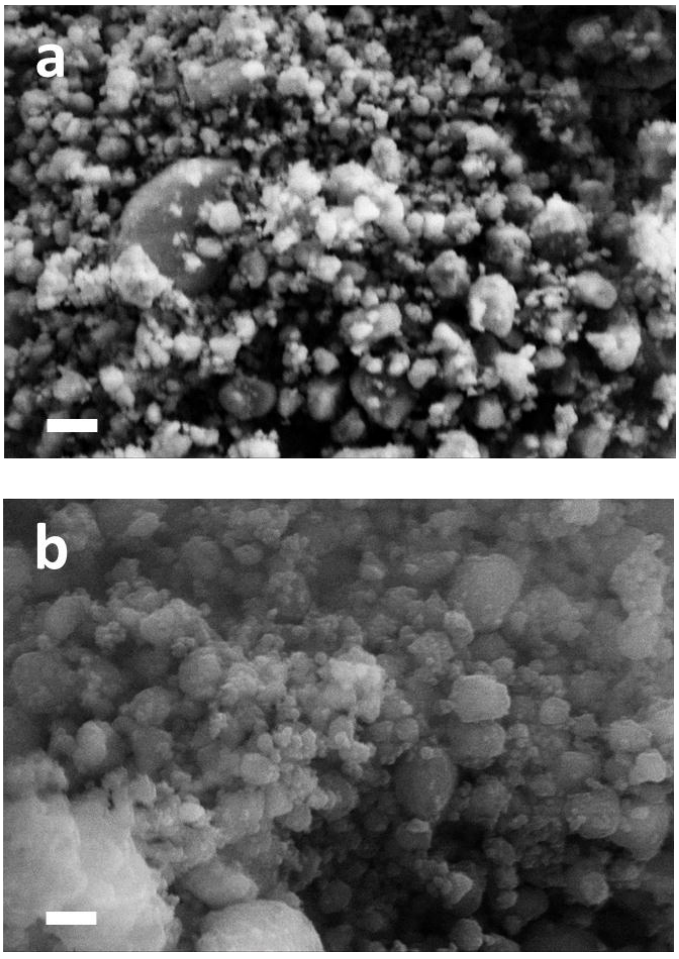

Figure 6.5 SEM images of a) ball-milled TaC prior to chlorination, scale bar is 500 nm; b) ball-milled TaC after chlorination, scale bar is 500 nm.

6.3.2.2 Surface area, pore size/volume measurements

The ball-milled nano-CDC's nitrogen isotherm is shown in **Figure 6.6a**. The isotherm is very similar to the bulk-CDC with a sharp nitrogen uptake at low pressure that is indicative of sufficient microporosity. The overall pore volume (1.61 cm^3 g^{-1}) and surface area (1939 m^2 g^{-1}) of nano-CDC is almost identical to bulk-CDC. This is expected as the particle size did not decrease sufficiently enough through ball-milling to introduce a substantial amount of new surface area. The pore size distribution of nano-CDC is shown in **Figure 6.6b** and is slightly different than bulk-CDC. There is more microporosity with a diameter < 1 nm, but there is also less pore volume from pores < 2 nm. The mesoporosity is similar to bulk-CDC and is most likely a contribution from interparticle mesopores.

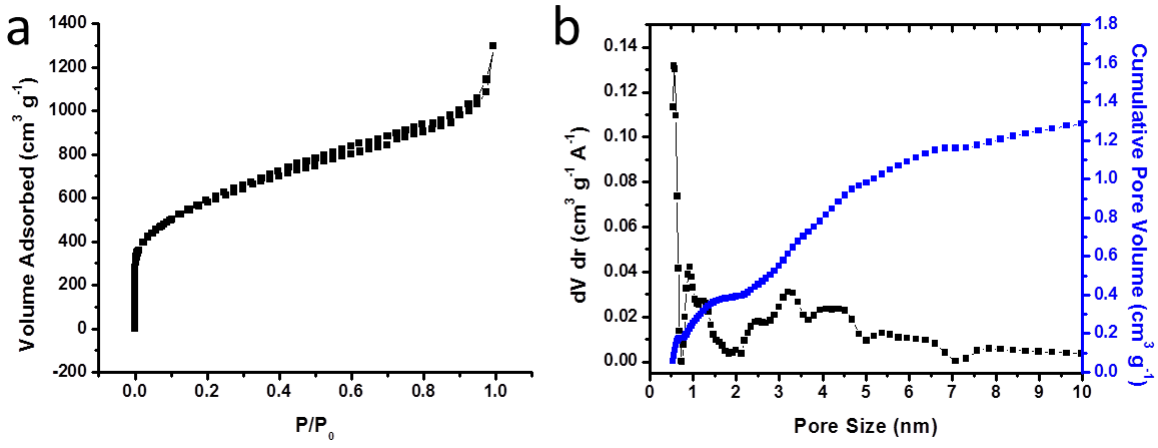

Figure 6.6 a) Nitrogen isotherm of nano-CDC; (b) Pore size distribution of nano-CDC.

6.3.2.3 Thermogravimetric analysis

The best electrochemical results were obtained with the agitation-friction method of sulfur infiltration with bulk-CDC. Therefore, this method was used to infiltrate 40 wt% sulfur into nano-CDC. The TGA curve for nano-CDC-AF is shown in **Figure 6.7**.

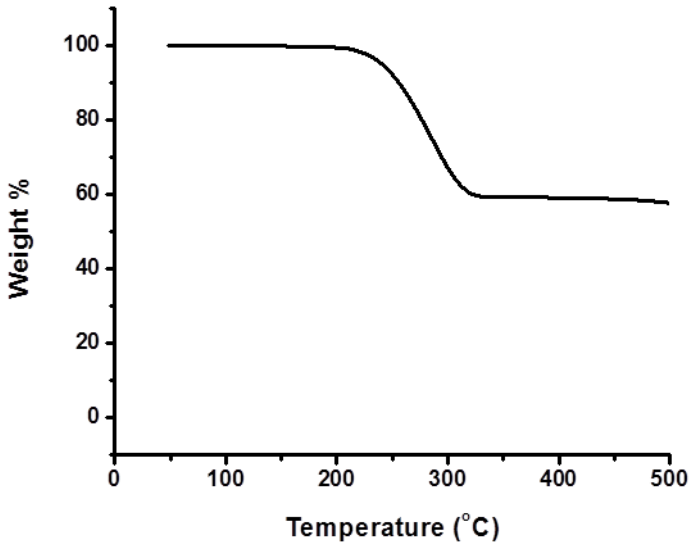

Figure 6.7 TGA curve (N_2 atmosphere) of nano-CDC-AF.

6.3.2.4 Electrochemical analysis

The electrochemical properties of nano-CDC-AF were tested under similar conditions to bulk-CDC-AF except the rate was increased from C/10 to C/2 and the voltage window was decreased from 3.0 – 1.5 V to 2.6 – 1.9 V. The rate was increased because parallel studies in the lab showed more stable cycling in the electrolyte (1M LiTFSI in DME:DOL) at increased current densities. The voltage window was narrowed because $LiNO_3$ was used in the electrolyte to protect the negative electrode but a report by Zhang *et al.* showed that $LiNO_3$ can undergo reduction on carbon below 1.8 V.[7] In order to limit reduction products that could block lithium ion mobility or increase cell impedance the voltage window was

narrowed. Shown in **Figure 6.8a** is the first cycle voltage profile of nano-CDC-AF. Even at an increased rate, the capacity approaches 1000 mA h g^{-1}_{sulfur}, but the cell still suffers from a lower first cycle charge capacity. The long term cycling performance (**Figure 6.8b**) is very poor and the cell experiences fast capacity fading over 15 cycles. It is readily apparent that both agitation-friction and melt-diffusion are ineffective at filling the micropores with sulfur.

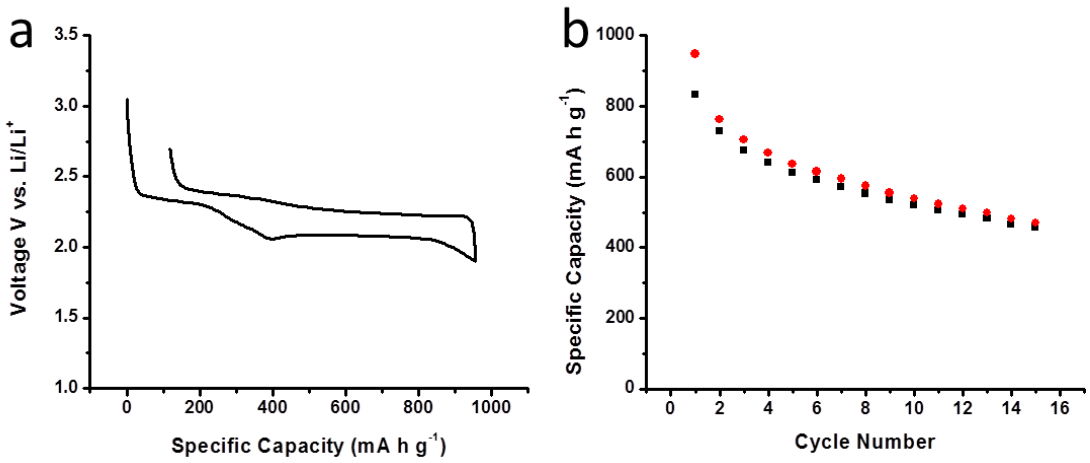

Figure 6.8 a) Galvanostatic voltage profile of the first cycle of nano-CDC-AF at C/2 rate; (b) Long term cycling of nano-CDC-AF at C/2 rate.

6.3.2.5 Thermogravimetric analysis

A new technique was developed to allow gas phase sulfur at high pressure to penetrate the CDC structure and fill the micropores with sulfur molecules. The technique is called vapour-infusion and subsequent samples will be labeled nano-CDC-VI-x (where x denotes the sulfur content). The nano-CDC is loaded into a narrow quartz tube with sulfur and is separated by glass wool. The tube is evacuated and sealed. The tube is heated to 600 °C where all of the sulfur is in the gas phase at high pressure. At this temperature

the gas is comprised of sulfur molecules from S_8 to S_2. This technique should allow deeper penetration of these smaller sulfur molecules into the interior of the nano-CDC. However, as shown in the TGA curve in **Figure 6.9**, the sulfur content is difficult to tune initially and an excess of sulfur is deposited (**Figure 6.9 black line**). After vapour-infusion the sulfur content can be tuned because the excess bulk sulfur evolves at a lower temperature than the highly confined sulfur. By heating the full infusion material to 280 °C under Ar flow, the majority of the excess sulfur is removed. Further treatment to 300 °C removes all of the excess low temperature sulfur leaving a composite with 41 wt% sulfur.

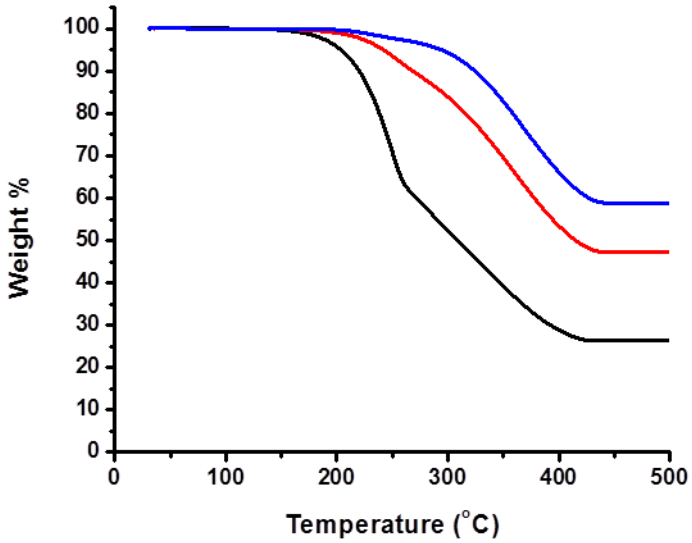

Figure 6.9 TGA curve (N_2 atmosphere) of nano-CDC-VI (a) full infusion (black); (b) reduced sulfur content 52 wt% (red); (c) reduced sulfur content 41 wt% (blue).

6.3.2.6 Electrochemical analysis

The electrochemical properties of nano-CDC-VI-52 and nano-CDC-VI-41 were examined in a coin cell configuration with the same electrolyte, voltage window and discharge/charge rate as in the previous section with nano-CDC-AF. The first cycle

voltage profile of both composites is shown in **Figure 6.10a**. The excess sulfur in nano-CDC-VI-52 is highly resistive and causes overpotential in the cell as well as a lower overall discharge capacity. The excess sulfur is postulated to be on the exterior of the carbon particles and is blocking to both lithium ions and electrons. When the excess sulfur is removed the overpotential lessens, an increase in discharge capacity occurs and there is also a complete re-oxidation of the sulfur upon charge. In the long term cycling (**Figure 6.10b**), nano-CDC-VI-41 maintains a larger discharge capacity over 100 cycles but experiences significant capacity fading that is almost identical to nano-CDC-VI-52.

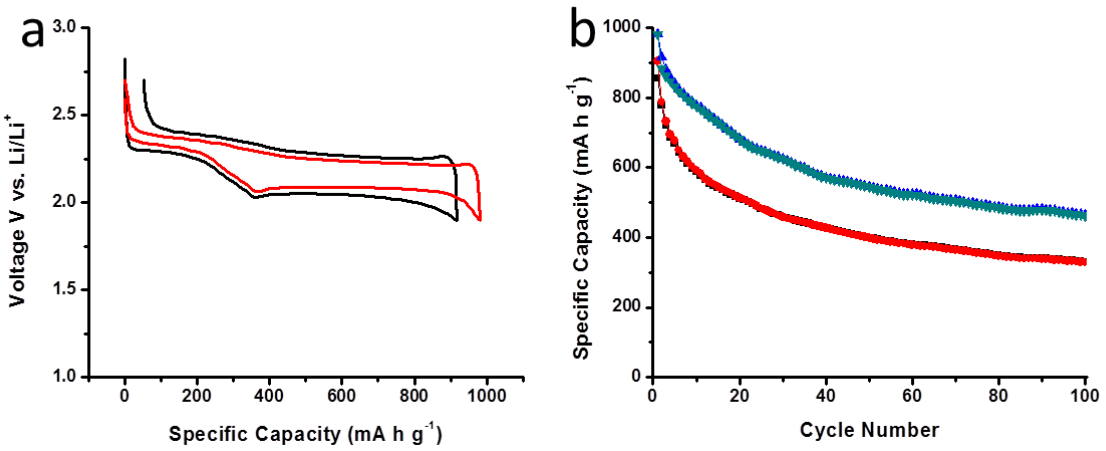

Figure 6.10 a) Galvanostatic voltage profile of the first cycle of nano-CDC-VI with 52 wt% sulfur (black) and 41 wt% sulfur (red) at C/2 rate; (b) Long term cycling of nano-CDC-VI with 52 wt% sulfur (discharge, red; charge, black) and 41 wt% sulfur (discharge, green; charge, blue) at C/2 rate.

The capacity fading in both cells is attributed to poor retention of lithium polysulfides at the positive electrode. Many recent reports highlight the importance of having hydrophilic groups[8,9] attached to the carbon host or hydrophilic additives[10,11] in the positive electrode. The hydrophilic groups interact with the lithium polysulfides and help

to contain them at the positive electrode. CDC's are pure carbon and contain no functional groups due to the special synthetic process. The lack of hydrophilic groups allows lithium polysulfides to be readily dissolved in the electrolyte and results in rapid capacity fading.

6.4 Conclusion

Microporous carbide derived carbons were successfully synthesized by chlorine treatment of a metal carbide. The aim of the research was to confine sulfur molecules in the micropores of the CDC in an attempt to limit active mass loss in the electrolyte. Bulk CDC was prepared and sulfur was impregnated into the structure through two methods with agitation-friction proving to be superior in terms of electrochemical properties. The particle size of the CDC was then reduced to allow sulfur access to more micropores in the particles. The electrochemistry remained poor with rapid capacity fading over 15 cycles. A new sulfur infiltration technique was developed that put sulfur into the CDC at high temperature and in the gas phase. This proved to increase the capacity retention of the cell and also allowed easy tuning of the sulfur content in the composite. CDC's proved to be too hydrophobic with no functional groups that could aid in retaining hydrophilic lithium polysulfides. This caused rapid capacity fading even at high rate cycling. Future work could focus on introducing functional groups on the surface of the CDC as well as introduce hydrophilic additives into the positive electrode composite.

Future Perspectives

The work presented in this thesis focussed on the positive electrode of the Li-S battery and little mention was given to the other two main components that comprise a battery: the negative electrode and the electrolyte. The reason for this is that the main issues hindering commercialization of the Li-S battery is the use of elemental sulfur at the positive electrode. In the first part of the thesis reduced graphene oxide was used as both a conductive additive and structure forming agent to envelop large micron sized sulfur particles. While this configuration allowed the highest ever reported sulfur content in the positive electrode, it suffered from low overall discharge capacity and capacity fading at relatively low rates. Future work to advance this material and improve its electrochemistry would be to tailor the hierarchical structure of the composite. Upon reduction of sulfur the structure can collapse and eliminate lithium ion diffusion paths as well as disconnect sulfur electrically from the current collector. Through the addition of a nano-sized inactive component, once sulfur is reduced and dissolved the inactive component helps to retain the open structure of the electrode composite and increase cycle life.

The second part of the thesis focussed on the use of mesoporous titania as an additive to the positive electrode of the Li-S battery. The advantage of this material is that it allows the use of a large pore mesoporous carbon that can be cycled at high rates and garner a large discharge capacity. Future research could concentrate on determining the optimum amount of mesoporous titania that is required in the electrode to maximize capacity retention. It is also important to research other metal oxides that can be synthesized with mesopores that could possibly have a more favourable interaction with lithium

polysulfides while still remaining as an electrochemically inactive component of the electrode.

In the next chapter 220 nm porous carbon spheres were synthesized with a hollow interior and porous shell. The spheres were impregnated through a melt-diffusion method with 68 wt% sulfur. The electrochemical properties of the material were excellent with greater than 100% capacity retention over 100 cycles at a 1C rate. The only downfall of the material was the low overall discharge capacity that could be attributed to the inaccessibility of sulfur due to almost complete filling of the porous shell. Future research could attempt to tailor the spheres architecture in an attempt to access more sulfur. The spheres shell could be made thicker to increase the pore volume contribution from the mesopores. This would allow an increase in sulfur content while also ensuring that the pores are not "stuffed" with sulfur which is the main cause of lower initial discharge capacities.

The last chapter attempted to confine sulfur in the micropores of a carbide derived carbon. The electrochemical properties were poor with micron sized CDC and improved slightly with a reduction in particle size. However, to produce the best electrochemistry a relatively complex technique was used to vapour-infuse sulfur into the micropores of the CDC. The conclusion drawn from this research was that CDC's are pure carbon and contain no hydrophilic functional groups that will positively interact with lithium polysulfides in an attempt to limit their dissolution in the electrolyte. Future research could address this pitfall through the addition of functional groups that are chemically or physically attached to the carbon. Oxidation of the carbon decreases conductivity, but

polymer coatings can act to hinder polysulfide mobility while maintaining a highly conductive network for electron conduction.

References

References Chapter 1

1 D. Peramunage and S. Licht, *Science*, **261**, 1029, (1993).

2 J. A. Dean, *Lange's Handbook of Chemistry*, McGraw-Hill, New York, (1985).

3 H. Yamin and E. Peled, *J. Power Sources*, **9**, 281, (1983).

4 J. I. Yamaki, S. I. Tobishima, Y. Sakurai, K. I. Saito and K. Hayashi, *J. Appl. Electrochem.*, **28**, 135, (1998).

5 S. E. Cheon, K. S. Ko, J. H. Cho, S. W. Kim, E. Y. Chin and H. T. Kim, *J. Electrochem. Soc.*, **150**, A800, (2003).

6 B. H. Jeon, J. H. Yeon, K. M. Kim and I. J. Chung, *J. Power Sources*, **109**, 89, (2002).

7 N. Tachikawa, K. Yamauchi, E. Takashima, J. Park, K. Dokko and M. Watanabe, *Chem. Commun.*, **47**, 8157, (2011).

8 X. Ji, K. T. Lee and L. F. Nazar, *Nature Mater.*, **8**, 500, (2009).

9 X. Li, Y. Cao, W. Qi, L. V. Saraf, J. Xiao, Z. Nie, J. Mietek, J. G. Zhang, B. Schwenzer and J. Liu, *J. Mater. Chem.*, **21**, 16603, (2011).

10 C. Liang, N. J. Dudney and J. Y. Howe, *Chem. Mater.*, **21**, 4724, (2009).

11 G. He, X. Ji and L. F. Nazar, *Energy & Environ. Sci.*, **4**, 2878, (2011).

12 S. R. Chen, Y. P. Zhai, G. L. Xu, Y. X. Jiang, D. Y. Zhao, J. T. Li, L. Huang and S. G. Sun, *Electrochim. Acta*, **56**, 9549 (2011).

13 J. Schuster, G. He, T. Bein and L. F. Nazar, *Angew. Chem.*, **51**, 3591, (2012).

14 N. Jayaprakash, J. Shen, S. S. Moganty, A. Corona and L. A. Archer, *Angew. Chem. Int. Ed.*, **50**, 5904, (2011).

15 B. Zhang, X. Qin, G. R. Li and X. P. Gao, *Energy & Environ. Sci.*, **3**, 1531, (2010).

16 J. Gao, M. A. Lowe, Y. Kiya and H. D. Abruña, *J. Phys. Chem. C*, **115**, 25132, (2011).

17 R. Elazari, G. Salitra, A. Garsuch, A. Panchenko and D. Aurbach, *Adv. Mater.*, **23**, 5641, (2011).

18 J. Z. Wang, L. Lu, M. Choucair, J. A. Stride, X. Xu and H. K. Liu, *J. Power Sources*, **196**, 7030, (2011).

19 H. Wang, Y. Yang, Y. Liang, J. T. Robinson, Y. Li, A. Jackson, Y. Cui and H. Dai, *Nano Lett.*, **11**, 2644, (2011).

20 Y. Cao, X. Li, Aksay, J. Lemmon, Z. Nie, Z. Yang and J. Liu, *Phys. Chem. Chem. Phys.*, **13**, 7660, (2011).

21 L. Ji, M. Rao, H. Zheng, L. Zhang, Y. Li, W. Duan, J. Guo, E. J. Cairns and Y. Zhang, *J. Am. Chem. Soc.*, **133**, 18522, (2011).

22 S. Evers and L. F. Nazar, *Chem. Commun.*, **48**, 1233, (2012).

23 Y. X. Wang, L. Huang, L. C. Sun, S. Y. Xie, G. L. Xu, S. R. Chen, Y. F. Xu, J. T. Li, S. L. Chou, S. X. Dou and S. G. Sun, *J. Mater. Chem.*, **22**, 4744, (2012).

24 W. Ahn, K. B. Kim, K. N. Jung, K. H. Shin and C. S. Jin, *J. Power Sources*, **202**, 394, (2012).

25 J. Guo, Y. Xu and C. Wang, *Nano Lett.*, **11**, 4288, (2011).

26 M. Rao, X. Song and E. J. Cairns, *J. Power Sources*, **205**, 474, (2012).

27 L. Ji, M. Rao, S. Aloni, L. Wang, E. J. Cairns and Y. Zhang, *Energy Environ. Sci.*, **4**, 5053, (2011).

28 G. Zheng, Y. Yang, J. J. Cha, S. S. Hong and Y. Cui, *Nano Lett.*, **11**, 4462, (2011).

29 L. Qiu, S. Zhang, L. Zhang, M. Sun and W. Wang, *Electrochim. Acta*, **55**, 4632, (2010).

30 X. Liang, Z. Wen, Y. Liu, X. Wang, H. Zhang, M. Wu and L. Huang, *Solid State Ionics*, **192**, 347, (2011).

31 X. Liang, Y. Liu, Z. Wen, L. Huang, X. Wang and H. Zhang, *J. Power Sources*, **196**, 6951, (2011).

32 L. Xiao, Y. Cao, J. Xiao, B. Schwenzer, M. H. Engelhard, L. V. Saraf, Z. Nie, G. J. Exarhos and J. Liu, *Adv. Mater.*, **24**, 1176, (2012).

33 L. Yin, J. Wang, J. Yang and Y. Nuli, *J. Mater. Chem.*, **21**, 6807, (2011).

34 R. Demir-Cakan, M. Morcette, F. Nouar, C. Davoisne, T. Devic, D. Gonbeau, R. Dominko, C. Serre, G. Férey and J. M. Tarascon, *J. Am. Chem. Soc.*, **133**, 16154, (2011).

35 F. Wu, J. Chen, R. Chen, S. Wu, L. Li, S. Chen and T. Zhao, *J. Phys. Chem. C*, **115**, 6057, (2011).

36 Y. Yang, G. Yu, J. J. Cha, H. Wu, M. Vosgueritchian, Y. Yao, Z. Bao and Y. Cui, *ACS Nano*, **5**, 9187, (2011).

37 F. Wu, J. Chen, L. Li, T. Zhao and R. Chen, *J. Phys. Chem. C*, **115**, 24411, (2011).

38 X. Ji, S. Evers, R. Black and L. F. Nazar, *Nature Commun.*, **2**, 325, (2011).

References Chapter 2

1 P.P. Ewald, Fifty Years of X-ray Diffraction, International Union of Crystallography, Utrecht, (1962).

2 L. V. Azaroff and M. J. Buerger, *The Powder Method in X-ray Crystallography*, McGraw-Hill Book Company Inc., New York, (1958).

3 W. L. Bragg, *Proc. Camb. Phil. Soc.*, **17**, 43, (1913).

4 C. Suryanarayana and M. Grant Norton, *X-Ray Diffraction A Practical Approach*, Plenum Press, New York, (1998).

5 B. E. Warren, *X-Ray Diffraction*, General Publishing Company Ltd., North York, ON, (1990).

6 S. Brunauer, P. H. Emmett and E. Teller, *J. Am. Chem. Soc.*, **60**, 309, (1938).

7 E. P. Barrett, L. G. Joyner and P. P. Halenda, *J. Am. Chem. Soc.*, **73**, 373, (1951).

References Chapter 3

1 H. Wang, Y. Yang, Y. Liang, J. T. Robinson, Y. Li, A. Jackson, Y. Cui and H. Dai, *Nano Lett.*, **11**, 2644, (2011).

2 J. Z. Wang, L. Lu, M. Choucair, J. A. Stride, X. Xu and H. K. Liu, *J. Power Sources,* **196**, 7030, (2011).

3 Y. Cao, X. Li, I. A. Aksay, J. Lemmon, Z. Nie, Z. Yang and J. Liu, *Phys. Chem. Chem. Phys.*, **13**, 7660, (2011).

4 N. I. Kovtyukhova, P. J. Ollivier, B. R. Martin, T. E. Mallouk, S. A. Chizhik, E. V. Buzaneva and A. D. Gorchinskiy, *Chem. Mater.*, **11**, 771, (1999).

5 X. Du, Z. Z. Yu, A. Dasari, J. Ma, M. Mo, Y. Meng and Y. W. Mai, *Chem Mater.*, **20**, 2066, (2008).

6 V. S. Kolosnitsyn, E. V. Kuzmina, E. V. Karaseva and S. E. Mochalov, *J. Power Sources*, **196**, 1478, 2011.

7 C. Hontoria-Lucas, A. López-González, M. Rojas-Cervantes and R. Martín-Aranda, *Carbon*, **33**, 1585, (1995).

8 A. Ward, *J. Phys. Chem.*, **72**, 4133, (1968).

9 S. Gupta, B. Weiner and G. J. Morell, *Appl. Phys.*, **92**, 5457, (2002).

10 A. Jorio, E. Martins Ferreira, M. Moutinho, F. Stavale, C. Achete and R. Capaz, *Phys. Status Solidi B*, **247**, 2980, (2010).

11 N. Jayaprakash, J. Shen, S. Moganty, A. Corona and L. A. Archer, *Angew. Chem. Int. Ed.*, **50**, 5904, (2011).

12 N. Tachikawa, K. Yamauchi, E. Takashima, J. W. Park and M. Watanabe, *Chem. Commun.*, **47**, 8157, (2011).

13 J. Hassoun and B. Scrosati, *Adv. Mater.*, **22**, 5198, (2010).

References Chapter 4

1 J. Shim, K. A. Striebel and E. J. Cairns, *J. Electrochem. Soc.*, **149**, A1321, (2002).

2 N. Tachikawa, K. Yamauchi, E. Takashima, J. W. Park, K. Dokko and M. Watanabe, *Chem. Commun.*, **47**, 8157, (2011).

3 E. Peled, A. Gorenshtein, M. Segal and Y. J. Sternberg, *J. Power Sources*, **26**, 269, (1989).

4 D. Aurbach, E. Pollak, R. Elazari, G. Salitra, C. S. Kelley and J. Affinito, *J. Electrochem. Soc.*, **156**, A694, (2009).

5 M. S. Hong, S. C. Han, H. S. Kim, J. H. Kim, K. T. Kim, Y. M. Kang, H. J. Ahn, S. X. Dou and J. Y. Lee, *J. Electrochem. Soc.*, **151**, A791, (2004).

6 Y. J. Choi, B. S. Jung, D. J. Lee, J. H. Jeong, K. W. Kim, H. J. Ahn, K. K. Cho and H. B. Gu, *Phys. Scr.*, **, T129**, 62, (2007).

7 X. Ji, S. Evers, R. Black and L. F. Nazar, *Nature Commun.***, 2**, 325, (2011).

8 C. Yu, J. Fan, B. Tian and D. Zhao, *Chem. Mater.*, **16**, 889, (2004).

9 A. Hegazy and E. Prouzet, *Chem. Mater.***, 24**, 245, (2012).

10 M. Holzapfel, A. Martinent, F. Alloin, B. Le Gorrec, R. Yazami and C. Montella, *J. Electroanal. Chem.***, 546**, 41, (2003).

11 M. Bailey and S. Donne, *J. Electrochem. Soc.***, 158**, A802, (2011).

12 J. A. Gladysz, V. K. Wong and B. S. Jick, *J. C. S. Chem. Commun.***,** 838, (1978).

References Chapter 5

1 X. Ji, K. T. Lee and L. F. Nazar, *Nature Materials*, **4**, 500, (2009).

2 C. Liang, N. Dudney and J. Howe, *Chem. Mater.*, **21**, 4724, (2009).

3 X. Ji, S. Evers and L. F. Nazar, *Nature Commun.*, **2**, 325, (2011).

4 G. He, X. Ji and L. F. Nazar, *Energy & Enviro. Sci.*, **4**, 2878, (2011).

5 X. Li, Y. Cao, W. Qi, L. Saraf, J. Xiao, Z. Nie, B. Schwenzer and J. Lui, *J. Mater. Chem.*, **21**, 16603, (2011)

6 N. Jayaprakash, J. Shen, S. Moganty, A. Corona and L. A. Archer, *Angew. Chem. Int. Ed.*, **50**, 5904, (2011).

7 A. Fuertes, P. Valle-Vigón and M. Sevilla, *Chem. Commun.*, **48**, 6124, (2012).

8 M. M. Bruno, N. G. Cotella, M. C. Miras and C. A. Barbero, *Colloids and Surfaces A: Physiochem. Eng. Aspects*, **362**, 28, (2010).

9 J. Guo, Y. Xu and C. Wang, *Nano Lett.*, **11**, 4288, (2011).

10 L. Xiao, Y. Cao, J. Xiao, B. Schwenzer, M. H. Engelhard, L. V. Saraf, Z. Nie, G. J. Exarhos and J. Liu, *Adv. Mater.*, **24**, 1176, (2012).

References Chapter 6

1 R. Elazari, G. Salitra, A. Garsuch, A. Panchenko and D. Aurbach, *Adv. Mater.*, **23**, 5641, (2011).

2 B. Zhang, X. Qin, G. R. Li and X. P. Gao, *Energy & Environ. Sci.*, **3**, 1531, (2010).

3 D. Wang, G. Zhou, F. Li, K. Wu, G. Lu, H. Cheng and I. R. Gentle, *Phys. Chem. Chem. Phys.*, **14**, 8703, (2012).

4 J. Chmiola, G. Yushin, Y. Gogotsi, C. Portet, P. Simon and P. L. Taberna, *Science*, **313**, 1760, (2006).

5 S. Urbonaite, J. M. Juárez-Galán, J. Leis, F. Rodríguez-Reinoso and G. Svensson, *Micro. and Meso. Mat.*, **113**, 14, (2008).

6 X. Ji, S. Evers, K. T. Lee and L. F. Nazar, *Chem. Commun.*, **46**, 1658, (2010).

7 S. S. Zhang, *Electro. Acta*, **70**, 344, (2012)

8 H. Wang, Y. Yang, Y. Liang, J. T. Robinson, Y. Li, A. Jackson, Y. Cui and H. Dai, *Nano Lett.*, **11**, 2644, (2011).

9 G. Zheng, Y. Yang, J. J. Cha, S. S. Hong and Y. Cui, *Nano Lett.*, **11**, 4462, (2011).

10 X. Ji, S. Evers, R. Black and L. F. Nazar, *Nature Commun.*, **2**, 325, (2011).

11 R. Demir-Cakan, M. Morcette, F. Nouar, C. Davoisne, T. Devic, D. Gonbeau, R. Dominko, C. Serre, G. Férey and J. M. Tarascon, *J. Am. Chem. Soc.*, **133**, 16154, (2011).